Journal of Computational Physics 513 (2024) 113190

Contents lists available at ScienceDirect

Journal of Computational Physics

journal homepage: www.elsevier.com/locate/jcp

Asymptotic preserving semi-Lagrangian discontinuous Galerkin methods for multiscale kinetic transport equations ☆

Yi Cai [a], Guoliang Zhang [b], Hongqiang Zhu [c], Tao Xiong [d,*]

[a] School of Mathematical Sciences, Xiamen University, Xiamen, Fujian 361005, PR China
[b] Institute of Natural Sciences, Shanghai Jiao Tong University, Shanghai 200240, PR China
[c] School of Natural Sciences, Nanjing University of Posts and Telecommunications, Nanjing, Jiangsu 210023, PR China
[d] School of Mathematical Sciences, University of Science and Technology of China, Hefei, Anhui 230026, PR China

ARTICLE INFO

Keywords:
Kinetic transport equation
Diffusive scaling
Asymptotic preserving
Semi-Lagrangian
Discontinuous Galerkin
Parallel computing

ABSTRACT

We propose a new family of asymptotic preserving (AP) discontinuous Galerkin (DG) schemes for kinetic transport equations under a diffusive scaling. They are built upon a characteristics-based model reformulation proposed in Zhang et al. (2023) [27]. The reformulated model comprises a convection-diffusion-like equation for the macroscopic density and another evolution equation for the distribution function. We employ the equations in a weak form to enjoy the advantages of a DG method. We also leverage a semi-Lagrangian (SL) approach to achieve higher efficiency than a fully implicit scheme without loss of unconditional stability. A damping technique is introduced to control spurious numerical oscillations for high-order DG methods. We establish formal AP and Fourier stability analyses for fully discrete schemes in a linear scenario. Numerical experiments, covering one-dimensional to three-dimensional in space problems, confirm the accuracy, AP property, uniformly unconditional stability, and high parallel efficiency of the proposed methods.

1. Introduction

Kinetic theory is very important in multi-scale modeling, which provides a fundamental framework to bridge the gap between microscopic and macroscopic scales. It has been widely used in neutron transport, radiative transport, rarefied gas dynamics, and other related fields [1,2]. In this work, we are interested in the kinetic transport equation with a diffusive scaling

$$\varepsilon \partial_t f + \boldsymbol{v} \cdot \nabla_{\boldsymbol{x}} f = \frac{1}{\varepsilon} Q(f). \tag{1.1}$$

Here the unknown $f(t, \boldsymbol{x}, \boldsymbol{v})$, depending on time $t \in \Omega_t \subset \mathbb{R}^+$, spatial position $\boldsymbol{x} \in \Omega_{\boldsymbol{x}} \subset \mathbb{R}^d$ and velocity $\boldsymbol{v} \in \Omega_{\boldsymbol{v}} \subset \mathbb{R}^d$ where $1 \le d \le 3$, represents the density distribution function of particles in the phase space. The operator Q describes the collision effect among particles or between particles and the medium. $\varepsilon > 0$ is the Knudsen number, defined as the ratio of a mean free path to a typical

☆ The first and the fourth authors are partially supported by National Key R&D Program of China No. 2022YFA1004500, NSFC grant No. 92270112, NSF of Fujian Province No. 2023J02003, and the Strategic Priority Research Program of Chinese Academy of Sciences Grant No. XDA25010400. The research of H. Zhu is partially sponsored by NSFC No. 12371435, and G. Zhang is partially supported by China Postdoctoral Science Foundation No. 2023M742284.

* Corresponding author.
E-mail addresses: yicaim@stu.xmu.edu.cn (Y. Cai), zglmath@sjtu.edu.cn (G. Zhang), zhuhq@njupt.edu.cn (H. Zhu), taoxiong@ustc.edu.cn (T. Xiong).

https://doi.org/10.1016/j.jcp.2024.113190
Received 19 November 2023; Received in revised form 28 April 2024; Accepted 6 June 2024

Available online 11 June 2024

spatial length, determining the flow regime. With the presence of ε in front of the time derivative of f, we focus on the long-time behavior of the physical system.

Developing an efficient numerical scheme for this high-dimensional kinetic problem (especially when $d = 3$) entails several challenges. Firstly, we need to design a scheme that is effective not only in the kinetic regime (when ε is away from zero) but also in the diffusive regime (when ε is close to zero). A naive numerical discretization might produce unphysical solutions in the diffusive limit [3–5]. One popular successful approach is to design asymptotic-preserving (AP) schemes [6–8]. The basic idea behind AP schemes is to ensure that the numerical method accurately captures the asymptotic limit of the mathematical model at the discrete level. For (1.1), an AP scheme must be a consistent discretization for the corresponding limiting diffusion equation as $\varepsilon \to 0$. There are various ways to construct an AP scheme, including diffusive relaxation method [9,10], penalization method [11], macro-micro decomposition [12,13], and exponential integration [14–16]. Secondly, both the transport and collision terms exhibit strong stiffness when ε is small, posing great challenges to efficient time discretization, especially in the high-dimensional case. On the one hand, a fully explicit scheme yields a stringent time step condition $\Delta t = \mathcal{O}(\varepsilon h)$ (h is the mesh size) for stability and accuracy [17,18]. On the other hand, although a fully implicit scheme can avoid a stability limitation on the time step, it is very costly to solve a large-scale system of linear equations at each time step, even with efficient iterative solvers [19,20]. In addition, several implicit-explicit (IMEX) schemes are developed to balance stability conditions and computational cost. For stability, AP IMEX schemes (e.g., [12,13]) require a parabolic time step $\Delta t = \mathcal{O}(h^2)$ when $\varepsilon \ll h$ and $\Delta t = \mathcal{O}(\varepsilon h)$ otherwise, see [21,22] for some rigorous analyses. To enhance stability in the diffusive regime, one can apply an explicit-implicit-null technique [10,23,24] or modify an existing AP scheme by implicitly discretizing diffusion-related terms [15,16,25,26]. However, it is worth noting that when the system departs from the diffusive regime, these stability-enhanced AP schemes retain ε-dependent stability condition $\Delta t = \mathcal{O}(\frac{\varepsilon^2}{\varepsilon/h-\lambda})$. When the system enters the intermediate regime with $\varepsilon = \mathcal{O}(h)$, the time step condition becomes $\Delta t = \mathcal{O}(h^2)$ again. This restriction is still not pleasant in real applications, particularly when the regime varies in the computational domain, for example, problems with a large-range-variant opacity [24,27].

To overcome the stability issue in the intermediate regime, Zhang et al. [27] propose a new approach to reformulate the model (1.1), and then design a class of finite difference schemes that is uniformly unconditionally stable in all regimes. In such a framework, an approximation model for the macroscopic density is derived by following characteristics and recovering both convection and diffusion processes. For the numerical scheme, the density is updated using a semi-Lagrangian (SL) finite difference scheme for convection and a linearly implicit finite difference discretization for diffusion. The resulting scheme is verified to be uniformly unconditionally stable based on a Fourier analysis. Once the macroscopic density is available, the high-dimensional distribution function is fully decoupled in velocity via a discrete velocity method[1] [28,29]. Due to constant velocities for the transport, this decoupled updating is very convenient for parallel computing to avoid data racing. Notably, the kinetic equation is solved at each discrete velocity via a linearly implicit finite difference scheme, which involves a set of small-scale sparse linear systems (only depends on the spatial discretization). This approach is also used to design an efficient Monte-Carlo method for radiative transfer equations [30].

In this work, we aim to develop an AP SL discontinuous Galerkin (DG) method for kinetic transport problems (1.1). Here in space, we use a discontinuous finite element approximation in a weak form. The original DG scheme was developed by Reed and Hill for neutron transport equations [31]. Since then, due to its advantages of compactness, easy h-p adaptivity, and flexibility in handling complicated geometries, it has been widely used to study stationary and non-stationary problems, e.g., [32–38]. In time, we follow characteristics by fully utilizing an SL framework which greatly benefits from constant velocities within the discrete ordinate method, especially for high dimensions. Besides an SL flux approximation for the density equation, we also employ an SL approach to solve the kinetic equation (1.1), inspired by [39–42]. For the diffusion part, a linearly implicit local DG method is used. In this case, we only need to solve one small-scale sparse linear system at each step or each stage. Compared to the finite difference scheme in [27], the discontinuous finite element method in a weak form has several advantages. Firstly, it is flexible for h-p adaptivity and able to be applied to irregular geometries with unstructured meshes. Secondly, in order to control the numerical oscillation for the second order DG method, we introduce a damping term as proposed in [43,44] instead of a slope limiter used in [27]. The damping approach is more convenient for implicit time discretization and performs better than a slope limiter in the diffusive regime. Thirdly, in the weak form, it is possible to perform an energy stability analysis as has been done in [22,23,45]. The new contribution of this work is how to handle the SL characteristic tracing in a finite element weak form for both the transport part in the density equation and the kinetic equation. The resulting scheme is more efficient and flexible than the previous finite difference scheme. At this moment, we still only establish formal AP and Fourier stability analyses for a fully discrete scheme of the two-velocity telegraph equation. An energy stability analysis is left as our ongoing work. Numerical experiments, from one-dimensional (1D) to three-dimensional (3D) in space problems, are performed to validate the accuracy, stability, and high parallel efficiency of our proposed approach.

The rest of the paper is organized as follows. In Section 2, we revisit the model equations and derive the approximation model in the general multi-dimensional case. The numerical methods for the approximation model are described in Section 3. Formal asymptotic and Fourier stability analyses are given in Section 4. We provide some numerical tests in Section 5, followed by a conclusion remark in Section 6.

[1] In the radiative transfer community, this is often referred to as the discrete ordinate method or S_N method.

2. Model reformulation

Let $\Omega_{\boldsymbol{v}} \subset \mathbb{R}^d$ be bounded and symmetric with respect to the origin of $\mathbb{R}^d$. Suppose that $f(\boldsymbol{v})$ locates in the Hilbert space $L^2(\Omega_{\boldsymbol{v}}; \mathrm{d}\mu)$, where μ is a Lebesgue measure such that $\int_{\Omega_{\boldsymbol{v}}} 1 \mathrm{d}\mu = 1$. We denote $\langle f_1, f_2 \rangle := \int_{\Omega_{\boldsymbol{v}}} f_1 f_2 \, \mathrm{d}\mu$ as the $L^2(\Omega_{\boldsymbol{v}})$ inner product, and $\langle f \rangle := \langle f, 1 \rangle$ as the average in $\Omega_{\boldsymbol{v}}$ of any μ-measurable function f. Due to the symmetry of $\Omega_{\boldsymbol{v}}$, we have that $\langle g \rangle = 0$ for any odd function $g(\boldsymbol{v})$.

In this paper, we are interested in two classes of kinetic transport equations. The first class is the two-velocity model in the 1D case. Let $\Omega_v = \{-1, 1\}$ and μ be a discrete measure. The following four collision operators are widely considered [6,13]:

$$\mathcal{Q}(f) = \langle f \rangle - f; \tag{2.1a}$$

$$\mathcal{Q}(f) = \langle f \rangle - f + A\varepsilon v \langle f \rangle, \quad |A\varepsilon| < 1; \tag{2.1b}$$

$$\mathcal{Q}(f) = \langle f \rangle - f + B\varepsilon v \left[\langle f \rangle^2 - (\langle f \rangle - f)^2 \right], \quad B > 0; \tag{2.1c}$$

$$\mathcal{Q}(f) = K \langle f \rangle^m (\langle f \rangle - f), \quad K > 0, \quad m \le 0. \tag{2.1d}$$

In particular, the kinetic equation (1.1) with collision (2.1a) is named the Goldstein-Taylor model or the telegraph equation. The second class consists of multi-dimensional linear transport equations with a collision operator

$$\mathcal{Q}(f) = \sigma_s(\langle f \rangle - f) - \varepsilon^2 \sigma_a f + \varepsilon^2 S, \tag{2.2}$$

where $\sigma_s(\boldsymbol{x}) > 0, \sigma_a(\boldsymbol{x}) \ge 0$, and $\sigma = \sigma_s + \varepsilon^2 \sigma_a$ are associated with scattering, absorption, and total transport coefficients, respectively. The term $S(\boldsymbol{x})$ represents the internal source of particles. In this case, the average operator can be written as $\langle \cdot \rangle = \frac{1}{|\Omega_{\boldsymbol{v}}|} \int_{\Omega_{\boldsymbol{v}}} \cdot \, \mathrm{d}\boldsymbol{v}$, where

$$\begin{aligned} &\Omega_v = [-1, 1], && |\Omega_v| = 2, && \text{for} \quad d = 1; \\ &\Omega_{\boldsymbol{v}} = \left\{ \boldsymbol{v} : v_x^2 + v_y^2 = 1 \right\}, && |\Omega_{\boldsymbol{v}}| = 2\pi, && \text{for} \quad d = 2; \\ &\Omega_{\boldsymbol{v}} = \left\{ \boldsymbol{v} : v_x^2 + v_y^2 + v_z^2 = 1 \right\}, && |\Omega_{\boldsymbol{v}}| = 4\pi, && \text{for} \quad d = 3. \end{aligned} \tag{2.3}$$

Such equations arise in neutron transport [46], radiative transfer [1], wave transport in random media [47], etc.

2.1. Macro-micro reformulation

The macro-micro decomposition provides an elegant way to reformulate the linear kinetic equation (1.1) and analyzes their asymptotic properties [12]. The basic idea is to use an orthogonal decomposition of f:

$$f = \Pi f + (I - \Pi) f = \rho + \varepsilon g, \quad \rho := \langle f \rangle, \quad \langle g \rangle = 0, \tag{2.4}$$

where I is the identity operator and $\Pi(\cdot) = \langle \cdot \rangle$ is an orthogonal operator from $L^2(\Omega_{\boldsymbol{v}}; \mathrm{d}\mu)$ onto the subspace spanned by all functions independent of $\boldsymbol{v}$. By acting Π and its orthogonal complement $I - \Pi$ on (1.1), we obtain

$$\partial_t \rho + \nabla_{\boldsymbol{x}} \cdot \langle \boldsymbol{v} g \rangle = \frac{1}{\varepsilon^2} \Pi(\mathcal{Q}(\rho + \varepsilon g)), \tag{2.5a}$$

$$\partial_t g + \frac{1}{\varepsilon}(I - \Pi)(\boldsymbol{v} \cdot \nabla_{\boldsymbol{x}} g) + \frac{1}{\varepsilon^2} \boldsymbol{v} \cdot \nabla_{\boldsymbol{x}} \rho = \frac{1}{\varepsilon^3}(I - \Pi)(\mathcal{Q}(\rho + \varepsilon g)). \tag{2.5b}$$

The solvability of f in (1.1) is equivalent to that of ρ and g in (2.5). Specifically, one can verify that as $\varepsilon \to 0$, the limiting density equation for collision operators (2.1a)-(2.1d) are

$$\partial_t \rho = \left\langle v^2 \right\rangle \partial_{xx} \rho, \quad \text{heat equation;} \tag{2.6a}$$

$$\partial_t \rho + A \left\langle v^2 \right\rangle \partial_x \rho = \left\langle v^2 \right\rangle \partial_{xx} \rho, \quad \text{advection-diffusion equation;} \tag{2.6b}$$

$$\partial_t \rho + B \left\langle v^2 \right\rangle \partial_x (\rho^2) = \left\langle v^2 \right\rangle \partial_{xx} \rho, \quad \text{viscous Burgers equation;} \tag{2.6c}$$

$$\partial_t \rho = \frac{\left\langle v^2 \right\rangle}{K(1 - m)} \partial_{xx} \rho, \quad \text{porous media equation.} \tag{2.6d}$$

For collision operator (2.2), the density ρ also obeys a diffusion equation when $\varepsilon \to 0$,

$$\partial_t \rho - \nabla_{\boldsymbol{x}} \cdot (\sigma_s^{-1} \boldsymbol{D} \nabla_{\boldsymbol{x}} \rho) = -\sigma_a \rho + S, \quad \boldsymbol{D} = \langle \boldsymbol{v} \otimes \boldsymbol{v} \rangle. \tag{2.7}$$

Here $\sigma_s^{-1} \boldsymbol{D}$ denotes a $d \times d$ diffusion coefficient matrix, and $\otimes$ is a Kronecker product. Particularly, with (2.3), the matrix $\boldsymbol{D}$ becomes a diagonal matrix $D\boldsymbol{I}$ where D is a constant and $\boldsymbol{I}$ is a $d \times d$ identity matrix. Specifically, we deduce $D = \frac{1}{3}$ for $d = 1, 3$ and $D = \frac{1}{2}$ for $d = 2$.

With appropriate IMEX time discretization strategies [12,13], one can solve the macro-micro system (2.5) in a sequentially explicit way which leads to an AP scheme. Furthermore, unconditional stability in the diffusive regime can be achieved by utilizing an extra artificial viscosity or based on Schur decomposition [23,26]. However, all the mentioned schemes treat the stiff nonlinear convection term $\frac{1}{\varepsilon}(I-\Pi)(\boldsymbol{v}\cdot\nabla_{\boldsymbol{x}}g)$ explicitly. This causes a time step restriction in the intermediate regime when this convection term is comparable to the diffusion term [23,45]. If we apply an implicit time discretization to this convection term, (2.5) would give rise to a large-scale linear system that couples ρ and g, thus introducing additional complexity compared to the original equation (1.1).

2.2. Semi-Lagrangian reformulation

To ensure a clear and concise description, we focus on the following equation with the simplest collision operator:

$$\partial_t f + \frac{1}{\varepsilon}\boldsymbol{v}\cdot\nabla_{\boldsymbol{x}} f = \frac{1}{\varepsilon^2}(\langle f\rangle - f). \tag{2.8}$$

Here $\Omega_{\boldsymbol{v}}$ is either a two-velocity space or a continuous velocity space in (2.3). To overcome the limitation of a macro-micro decomposition system, we start with a macro-micro system comprising the following set of equations for ρ and f:

$$\partial_t \rho + \frac{1}{\varepsilon}\nabla_{\boldsymbol{x}}\cdot\langle \boldsymbol{v} f\rangle = 0, \tag{2.9a}$$

$$\partial_t f + \frac{1}{\varepsilon}\boldsymbol{v}\cdot\nabla_{\boldsymbol{x}} f = \frac{1}{\varepsilon^2}(\rho - f). \tag{2.9b}$$

As approaching the equilibrium, the microscopic equation (2.9b) becomes $f=\rho$ for all $\boldsymbol{v}\in\Omega_{\boldsymbol{v}}$ and the macroscopic equation (2.9a) cannot converge to the correct asymptotic limit. To capture the diffusive limit, the key idea is to reformulate the macroscopic flux $\boldsymbol{F} := \frac{1}{\varepsilon}\langle \boldsymbol{v} f\rangle$, which should recover a diffusion flux for the diffusive limit [27,30].

To begin with, we rewrite the kinetic equation (2.9b) in the following characteristic form

$$\frac{\mathrm{d}f}{\mathrm{d}t} = \frac{1}{\varepsilon^2}(\rho - f), \tag{2.10a}$$

$$\frac{\mathrm{d}\boldsymbol{x}}{\mathrm{d}t} = \frac{\boldsymbol{v}}{\varepsilon}, \tag{2.10b}$$

with d/dt being a material derivative. Without loss of generality, we set $t\in[t_0,t_1]$. For notations, we denote $\boldsymbol{x}_a = \boldsymbol{x}(t_a)$ for $a=0,1$ and $u(t)=u(t,\boldsymbol{x}(t))$ for $u=f,\rho,\partial_t\rho,\nabla_{\boldsymbol{x}}\rho$. Starting from $t=t_1$, a backward tracing of the characteristic line is

$$\boldsymbol{x}(t) = \boldsymbol{x}_1 - \frac{t_1-t}{\varepsilon}\boldsymbol{v}, \quad \forall t\in[t_0,t_1]. \tag{2.11}$$

By multiplying (2.10a) with an exponential factor e^{t/ε^2} and integrating over $[t_0,t_1]$, we obtain

$$f(t_1) = e^{-(t_1-t_0)/\varepsilon^2} f(t_0) + \int_{t_0}^{t_1} \frac{1}{\varepsilon^2} e^{-(t_1-t)/\varepsilon^2}\rho(t)\mathrm{d}t. \tag{2.12}$$

Integrating by parts for the time integral in (2.12), we get

$$f(t_1) = \rho(t_1) + e^{-(t_1-t_0)/\varepsilon^2}(f(t_0)-\rho(t_0)) - \int_{t_0}^{t_1} e^{-(t_1-t)/\varepsilon^2}\frac{\mathrm{d}\rho}{\mathrm{d}t}(t)\mathrm{d}t. \tag{2.13}$$

According to (2.4), we have $g=(f-\rho)/\varepsilon$, and it yields

$$g(t_1) = e^{-(t_1-t_0)/\varepsilon^2} g(t_0) - \frac{1}{\varepsilon}\int_{t_0}^{t_1} e^{-(t_1-t)/\varepsilon^2}\frac{\mathrm{d}\rho}{\mathrm{d}t}(t)\mathrm{d}t. \tag{2.14}$$

For the time integral in (2.14), applying the following approximation,

$$\int_{t_0}^{t_1} e^{-(t_1-t)/\varepsilon^2}\frac{\mathrm{d}\rho}{\mathrm{d}t}(t)\mathrm{d}t \approx \left(\int_{t_0}^{t_1} e^{-(t_1-t)/\varepsilon^2}\mathrm{d}t\right)\left.\frac{\mathrm{d}\rho}{\mathrm{d}t}\right|_{t=t_1} = \varepsilon^2(1-e^{-(t_1-t_0)/\varepsilon^2})\left.\frac{\mathrm{d}\rho}{\mathrm{d}t}\right|_{t=t_1}, \tag{2.15}$$

together with

$$\frac{\mathrm{d}\rho}{\mathrm{d}t}(t) = \partial_t\rho(t) + \frac{1}{\varepsilon}\boldsymbol{v}\cdot\nabla_{\boldsymbol{x}}\rho(t), \tag{2.16}$$

we deduce

$$g(t_1) = e^{-(t_1-t_0)/\varepsilon^2} g(t_0) - \varepsilon(1-e^{-(t_1-t_0)/\varepsilon^2})\partial_t\rho(t_1) - (1-e^{-(t_1-t_0)/\varepsilon^2})(\boldsymbol{v}\cdot\nabla_{\boldsymbol{x}}\rho)(t_1). \tag{2.17}$$

By taking the first moment of (2.17) in $\Omega_{\boldsymbol{v}}$, we obtain the approximation flux $\boldsymbol{G}$ at time t_1:

$$\boldsymbol{F}(t_1) = \frac{1}{\varepsilon}\langle \boldsymbol{v} f(t_1)\rangle = \langle \boldsymbol{v} g(t_1)\rangle \approx \boldsymbol{G}(t_1) := e^{-(t_1-t_0)/\varepsilon^2}\langle \boldsymbol{v} g(t_0)\rangle - (1-e^{-(t_1-t_0)/\varepsilon^2})(\boldsymbol{D}\nabla_{\boldsymbol{x}}\rho)(t_1). \tag{2.18}$$

Here $\boldsymbol{D}$ is the same as in (2.7). As we can see, the first term contributes to the convection process, while the second term is associated with the diffusion process. We can easily verify that when $\varepsilon \to 0$, the contribution of convection diminishes, while $\boldsymbol{G}$ converges to the diffusion flux, i.e., $\boldsymbol{G} \to \boldsymbol{D}\nabla_{\boldsymbol{x}}\rho$.

Suppose we would like to integrate (2.9) up to a fixed time T. We assume discrete time steps $t^n\,(n = 0, 1, \ldots)$ for the time interval $[0, T]$, and take a uniform step size $\Delta t = t^{n+1} - t^n$. In the SL framework, particles are tracked within a single time step, rather than throughout their entire motion in the fully Lagrangian framework. Setting $t_1 = t, \boldsymbol{x}_1 = \boldsymbol{x}, t_0 = t^n$, $\boldsymbol{x}_0 = \boldsymbol{x}^n = \boldsymbol{x} - \boldsymbol{v}(t - t^n)/\varepsilon$ and substituting (2.18) into (2.9a), we obtain an SL approximation for (2.9):

$$\partial_t \rho + e^{-(t-t^n)/\varepsilon^2}\nabla_{\boldsymbol{x}} \cdot \langle \boldsymbol{v} g(t^n, \boldsymbol{x}^n, \boldsymbol{v})\rangle = (1 - e^{-(t-t^n)/\varepsilon^2})\nabla_{\boldsymbol{x}} \cdot (\boldsymbol{D}\nabla_{\boldsymbol{x}}\rho), \tag{2.19a}$$

$$\partial_t f + \frac{1}{\varepsilon}\boldsymbol{v} \cdot \nabla_{\boldsymbol{x}} f = \frac{1}{\varepsilon^2}(\rho - f), \tag{2.19b}$$

where

$$g(t^n, \boldsymbol{x}^n, \boldsymbol{v}) = (f(t^n, \boldsymbol{x}^n, \boldsymbol{v}) - \rho(t^n, \boldsymbol{x}^n))/\varepsilon. \tag{2.20}$$

Our modeling decomposes the transport process into two parts: convection and diffusion. In particular, the convection term involves a backward tracing of microscopic perturbation g along the characteristic line, eliminating a scale-related time step limitation. The weight functions, represented as $\omega_1 = e^{-(t-t^n)/\varepsilon^2}$ and $\omega_2 = 1 - e^{-(t-t^n)/\varepsilon^2}$, balance the contribution of convection and diffusion. When ε is away from zero, both convection and diffusion are taken into account. When ε is close to zero, (2.19) becomes diffusion-dominated and formally converges to

$$\partial_t \rho = \nabla_{\boldsymbol{x}} \cdot (\boldsymbol{D}\nabla_{\boldsymbol{x}}\rho), \quad f = \rho. \tag{2.21}$$

This also shows that the new model preserves the desired diffusive limit. Theorem 2.2 below provides a new modeling error estimate that is more accurate than the one presented in [27]. Furthermore, this new error estimate offers insights into the order reduction observed in our numerical tests, see Section 5. To maintain the m-th order convergence rate, it is necessary to take $\Delta t = \varepsilon^{\frac{3}{2}} h^{\frac{m}{2}}$ and $h^m \le \varepsilon$, where h is the mesh size. For the sake of readability, we include the proofs for Lemma 2.1 and Theorem 2.2 in the appendix. In addition, extending the proposed modeling approach to other collision operators is feasible but may involve some tricks, see [27] for more details.

Lemma 2.1. *Suppose that a function $\eta = \eta(\tau)$ is smooth enough and there exists a uniform bound $M > 0$ such that $\left|\beta^{k+1}\eta^{(k)}(\tau)\right| \le M$ for all $k \ge 1$ and $\tau \in [0, s]$, where $0 < \beta \le 1$ is a given constant and $\eta^{(k)}(s)$ is the k-th derivative at a point $s > 0$. For $\alpha > 0$, the following error estimate holds:*

$$\left| \int_0^s e^{-\alpha(s-\tau)}(\eta(\tau) - \eta(s))d\tau \right| \le MU(\alpha, \beta, s), \tag{2.22}$$

where

$$U(\alpha, \beta, s) = \begin{cases} e^{-\alpha s} - 1 + \alpha s, & \alpha\beta = 1; \\ \frac{(\alpha\beta)^{-2}(1-e^{-\alpha s})}{1-(\alpha\beta)^{-1}} + \frac{(\alpha\beta)^{-1}(e^{-\alpha s} - e^{-(\alpha-\beta^{-1})s})}{1-(\alpha\beta)^{-1}}, & \alpha\beta \ne 1. \end{cases} \tag{2.23}$$

Theorem 2.2. *Let $0 < \varepsilon \le 1$, $t \in [t_0, t_1]$ and $\Delta t = t_1 - t_0$. Suppose that there exists a uniform upper bound $M > 0$ such that for all $k \ge 1$ and $t \in [t_0, t_1]$,*

$$\left|(\varepsilon\partial_t + \boldsymbol{v} \cdot \nabla_{\boldsymbol{x}})^{k+1}\rho(t)\right| \le M. \tag{2.24}$$

Then, the following error estimate holds for the flux approximation (2.18):

$$\|\boldsymbol{F} - \boldsymbol{G}\|_\infty \le CW^*(\varepsilon, \Delta t), \quad W^*(\varepsilon, \Delta t) = \begin{cases} \frac{\Delta t^2}{2\varepsilon^3}, & \text{if } \Delta t \le \varepsilon^2; \\ \frac{\varepsilon}{1-\varepsilon}, & \text{if } \Delta t > \varepsilon^2, \end{cases} \tag{2.25}$$

where $C > 0$ is a constant independent of ε and Δt but depends on M and velocity space $\Omega_{\boldsymbol{v}}$.

3. Numerical method

In this section, we will present our methods for the approximation model (2.19). For the convection part in both the macroscopic equation (2.19a) and the microscopic equation (2.19b), we use an SL approach with an upwind DG approximation in space. For the diffusion part in the macroscopic equation (2.19a), an implicit LDG approximation is taken. The main challenging part is the convection in (2.19a): although an implicit time discretization is used, the solution for a DG approximation is defined at the previous time level t^n due to an SL tracking.

We first review some notations for a DG method. We assume a quasi-uniform mesh $\mathcal{T}_h$ with its boundary Γ_h, namely, there exists a constant $c_0 > 0$ such that

$$h \le c_0 r, \quad h = \max_{K\in\mathcal{T}_h} h_K, \quad r = \max_{K\in\mathcal{T}_h} r_K, \tag{3.1a}$$

$$h_K = \mathrm{diam}(K), \quad r_K = \max\{\mathrm{diam}(S);\ S \text{ is a ball contained in } K\}. \tag{3.1b}$$

Then we consider a piecewise polynomial space on $\mathcal{T}_h$ as

$$U_h^k = \left\{ u \in L^2(\Omega_{\boldsymbol{x}});\ u\Big|_K \in \mathcal{P}^k(K), \quad \forall K \in \mathcal{T}_h \right\}. \tag{3.2}$$

Here $\mathcal{P}^k(K)$ is the set of all polynomials of degree at most k on K. We also introduce

$$V_h^k = \left\{ u(\cdot,\boldsymbol{v}) \in U_h^k;\ \int_{\Omega_{\boldsymbol{v}}}\int_{\Omega_{\boldsymbol{x}}} |u(\boldsymbol{x},\boldsymbol{v})|^2\,\mathrm{d}\boldsymbol{x}\mathrm{d}\boldsymbol{v} < \infty \right\}. \tag{3.3}$$

For a point $\boldsymbol{x}$ on the cell boundary ∂K with a unit outer normal vector $\boldsymbol{n}$, we denote its pointwise limits along $\boldsymbol{n}$ and $-\boldsymbol{n}$ by $\boldsymbol{x}^+$ and $\boldsymbol{x}^-$, respectively. We also define the jump and average of a function $u \in U_h^k$ at $\boldsymbol{x}$ along the normal vector as

$$[\![u]\!](\boldsymbol{x}) = u(\boldsymbol{x}^+) - u(\boldsymbol{x}^-), \quad \{\{u\}\}(\boldsymbol{x}) = \frac{1}{2}\left(u(\boldsymbol{x}^+) + u(\boldsymbol{x}^-)\right). \tag{3.4}$$

3.1. An implicit LDG method for the macroscopic equation

The macroscopic equation (2.19a) is close to a convection-diffusion equation, where the convection term has already been traced back to time level t^n by an SL method. First, we rewrite (2.19a) as a system only containing first-order derivatives

$$\boldsymbol{q} = \boldsymbol{D}\nabla_{\boldsymbol{x}}\rho, \tag{3.5a}$$

$$\partial_t \rho + e^{-(t-t^n)/\epsilon^2}\nabla_{\boldsymbol{x}}\cdot\left\langle \boldsymbol{v} S_{\boldsymbol{v}}^n[g]\right\rangle = (1-e^{-(t-t^n)/\epsilon^2})\nabla_{\boldsymbol{x}}\cdot\boldsymbol{q}. \tag{3.5b}$$

Here for clarity of notation, we introduce an SL evolution operator

$$S_{\boldsymbol{v}}^n[g](\boldsymbol{x},\boldsymbol{v}) = g(t^n, \boldsymbol{x} - \boldsymbol{v}\Delta t/\epsilon, \boldsymbol{v}). \tag{3.6}$$

With superscript n, we emphasize that $S_{\boldsymbol{v}}^n[g]$ is determined by the values of g at time level t^n.

We start with a temporal discretization. In order to overcome the parabolic time stability condition in the diffusive regime, we intend to treat the diffusion term implicitly. Besides, the convection term will be treated via a backward SL approach to eliminate stiffness. For high-order time discretizations, we utilize the backward differential formula (BDF). The resulting first- and second-order temporal discretizations are shown as follows:

- **First-order backward Euler scheme**

$$\boldsymbol{q}^{n+1} = \boldsymbol{D}\nabla_{\boldsymbol{x}}\rho^{n+1}, \tag{3.7a}$$

$$\frac{\rho^{n+1}-\rho^n}{\Delta t} + e^{-\Delta t/\epsilon^2}\nabla_{\boldsymbol{x}}\cdot\left\langle \boldsymbol{v} S_{\boldsymbol{v}}^n[g]\right\rangle = (1-e^{-\Delta t/\epsilon^2})\nabla_{\boldsymbol{x}}\cdot\boldsymbol{q}^{n+1}, \tag{3.7b}$$

- **Second-order BDF scheme**

$$\boldsymbol{q}^{n+1} = \boldsymbol{D}\nabla_{\boldsymbol{x}}\rho^{n+1}, \tag{3.8a}$$

$$\frac{3\rho^{n+1}-4\rho^n+\rho^{n-1}}{2\Delta t} + e^{-\Delta t/\epsilon^2}\nabla_{\boldsymbol{x}}\cdot\left\langle \boldsymbol{v} S_{\boldsymbol{v}}^n[g]\right\rangle = (1-e^{-\Delta t/\epsilon^2})\nabla_{\boldsymbol{x}}\cdot\boldsymbol{q}^{n+1}. \tag{3.8b}$$

In space, we take a DG approximation for the convection term and an LDG approximation for the diffusion term. A fully discrete scheme with first-order temporal accuracy is given as follows. Given $f_h^n \in V_h^k$, $\rho_h^n \in U_h^k$ and $g_h^n = (f_h^n - \rho_h^n)/\epsilon$, we look for $\rho_h^{n+1} \in U_h^k$, $\boldsymbol{q}_h^{n+1} \in (U_h^k)^d$ such that for any $K \in \mathcal{T}_h$, $\varphi \in U_h^k$, $\phi \in U_h^k$,

$$(\boldsymbol{q}_h^{n+1},\varphi)_K = \boldsymbol{D}\, r_K(\rho_h^{n+1},\varphi), \tag{3.9a}$$

$$\left(\frac{\rho_h^{n+1}-\rho_h^n}{\Delta t},\phi\right)_K + e^{-\Delta t/\epsilon^2}\, b_K(\left\langle \boldsymbol{v}S_{\boldsymbol{v}}^n[g_h]\right\rangle,\phi) = (1-e^{-\Delta t/\epsilon^2})\, l_K(\boldsymbol{q}_h^{n+1},\phi). \tag{3.9b}$$

Here $(\phi,\varphi)_K = \int_K \phi(\boldsymbol{x})\varphi(\boldsymbol{x})\mathrm{d}\boldsymbol{x}$ and the bilinear forms in the scheme are

$$r_K(\rho,\varphi) = \sum_{e\in\partial K}\int_e \boldsymbol{n}_{e,K}\check{\rho}_{e,K}\,\varphi\,\mathrm{d}\Gamma - \int_K \rho\nabla_{\boldsymbol{x}}\varphi\,\mathrm{d}\boldsymbol{x}, \tag{3.10a}$$

$$l_K(\boldsymbol{q},\phi) = \sum_{e\in\partial K}\int_e \boldsymbol{n}_{e,K}\cdot\hat{\boldsymbol{q}}_{e,K}\,\phi\,\mathrm{d}\Gamma - \int_K \boldsymbol{q}\nabla_{\boldsymbol{x}}\phi\,\mathrm{d}\boldsymbol{x}, \tag{3.10b}$$

$$b_K(\left\langle \boldsymbol{v}S_{\boldsymbol{v}}^n[g]\right\rangle,\phi) = \sum_{e\in\partial K}\int_e \left\langle \widetilde{\boldsymbol{v}S_{\boldsymbol{v}}^n[g]}\right\rangle_{e,K}\cdot\boldsymbol{n}_{e,K}\,\phi\,\mathrm{d}\Gamma - \int_K \left\langle \boldsymbol{v}S_{\boldsymbol{v}}^n[g]\right\rangle\cdot\nabla_{\boldsymbol{x}}\phi\,\mathrm{d}\boldsymbol{x}, \tag{3.10c}$$

where $\boldsymbol{n}_{e,K}$ is a unit outer normal vector to the edge e from the element K. $\check{\rho}_{e,K}^{(i)}$, $\hat{q}_{e,K}^{(i)}$, $\widetilde{\boldsymbol{v}S_{\boldsymbol{v}}^n[g]}_{e,K}$ are numerical fluxes. The integrals in (3.10c) are the most difficult parts that need very careful treatments. In short, $S_{\boldsymbol{v}}^n[g]$ is reconstructed on the upstream element K^* obtained by tracking an element K, while the test function ϕ is defined on K. We will discuss these integrals afterward. For the convection operator $\boldsymbol{v}S_{\boldsymbol{v}}^n[g]$, we use an upwind flux which is defined as

$$(\widetilde{\boldsymbol{v}S_{\boldsymbol{v}}^n[g]})_{e,K}(\boldsymbol{x}) = \boldsymbol{v}\{\{S_{\boldsymbol{v}}^n[g]\}\}_{e,K} - \frac{|\boldsymbol{v}|}{2}[\![S_{\boldsymbol{v}}^n[g]]\!]_{e,K} = \begin{cases} \boldsymbol{v}S_{\boldsymbol{v}}^n[g](\boldsymbol{x}^+), & \boldsymbol{v}\cdot\boldsymbol{n}_{e,K}>0;\\ \boldsymbol{v}S_{\boldsymbol{v}}^n[g](\boldsymbol{x}^-), & \boldsymbol{v}\cdot\boldsymbol{n}_{e,K}<0. \end{cases} \tag{3.11}$$

The pairs $(\check{\rho},\hat{\boldsymbol{q}})$ are consistent numerical fluxes related to the diffusion operator. Here, we can take either of the following fluxes:

$$\text{alternating left-right:}\quad \check{\rho}(\boldsymbol{x}) = \rho(\boldsymbol{x}^-),\quad \hat{\boldsymbol{q}}(\boldsymbol{x}) = \boldsymbol{q}(\boldsymbol{x}^+); \tag{3.12a}$$

$$\text{alternating right-left:}\quad \check{\rho}(\boldsymbol{x}) = \rho(\boldsymbol{x}^+),\quad \hat{\boldsymbol{q}}(\boldsymbol{x}) = \boldsymbol{q}(\boldsymbol{x}^-); \tag{3.12b}$$

$$\text{central:}\quad \check{\rho}(\boldsymbol{x}) = \frac{1}{2}(\rho(\boldsymbol{x}^-)+\rho(\boldsymbol{x}^+)),\quad \hat{\boldsymbol{q}}(\boldsymbol{x}) = \frac{1}{2}(\boldsymbol{q}(\boldsymbol{x}^-)+\boldsymbol{q}(\boldsymbol{x}^+)). \tag{3.12c}$$

In our numerical experiments, the alternating left-right flux is used.

Similarly, the fully discrete scheme with second-order temporal accuracy is shown here. The sole distinction from (3.9) lies in the first term on the left-hand side of (3.13b). Given $f_h^n\in V_h^k$, $\rho_h^{n-1}\in U_h^k, \rho_h^n\in U_h^k$ and $g_h^n = (f_h^n-\rho_h^n)/\varepsilon$, we look for $\rho_h^{n+1}\in U_h^k$, $\boldsymbol{q}_h^{n+1}\in (U_h^k)^d$ such that for any $K\in\mathcal{T}_h$, $\varphi\in U_h^k$, $\phi\in U_h^k$,

$$(\boldsymbol{q}_h^{n+1},\varphi)_K = \boldsymbol{D}\, r_K(\rho_h^{n+1},\varphi), \tag{3.13a}$$

$$\left(\frac{3\rho_h^{n+1}-4\rho_h^n+\rho_h^{n-1}}{2\Delta t},\phi\right)_K + e^{-\Delta t/\epsilon^2}\, b_K(\left\langle \boldsymbol{v}S_{\boldsymbol{v}}^n[g_h]\right\rangle,\phi) = (1-e^{-\Delta t/\epsilon^2})\, l_K(\boldsymbol{q}_h^{n+1},\phi). \tag{3.13b}$$

3.2. An SL DG method for the microscopic equation

For the microscopic equation (2.19b), with the density ρ obtained from the macroscopic equation (2.19a), we can treat it as a transport type equation with a given source term. For this transport equation, we apply a backward SL DG scheme by following the idea in [48,41].

We denote $K(t)$ as a dynamic element associated with Eulerian element K at time level t whose trajectory is bounded by characteristic lines. For example, if K is a 2D rectangle with nodes $\{\hat{\boldsymbol{x}}_i\}_{i=1}^4$, due to a constant velocity $\boldsymbol{v}/\varepsilon$, $K(t)$ is also a 2D rectangle with nodes $\{\boldsymbol{x}_i(t)\}_{i=1}^4$, where $\boldsymbol{x}_i(t) = \hat{\boldsymbol{x}}_i - (t^{n+1}-t)\boldsymbol{v}/\varepsilon$. Here we put K on the time level t^{n+1}, namely, $K^{n+1} = K(t^{n+1}) = K$, and denote $K^n = K(t^n) = K^*$ for the snapshot at time level t^n. We define a time dependent test function $\Psi(t,\boldsymbol{x})$ by the following adjoint final-value problem:

$$\partial_t\Psi + \frac{1}{\varepsilon}\boldsymbol{v}\cdot\nabla_{\boldsymbol{x}}\Psi = 0,\quad \Psi(t^{n+1},\boldsymbol{x}) = \psi(\boldsymbol{x}),\quad \forall\psi(\boldsymbol{x})\in U_h^k. \tag{3.14}$$

Solving (3.14) by utilizing the method of characteristics gives

$$\Psi(t,\boldsymbol{x}) = \psi(\boldsymbol{x}-\boldsymbol{v}(t^{n+1}-t)/\varepsilon),\quad \forall t\in[t^n,t^{n+1}]. \tag{3.15}$$

In particular, the test functions at time level t^{n+1} and t^n are

$$\Psi^{n+1}(\boldsymbol{x}) = \Psi(t^{n+1},\boldsymbol{x}) = \psi(\boldsymbol{x})\quad\text{and}\quad \Psi^n(\boldsymbol{x}) = \Psi(t^n,\boldsymbol{x}) = \psi(\boldsymbol{x}-\boldsymbol{v}\Delta t/\varepsilon). \tag{3.16}$$

Applying Reynold's transport theorem and divergence theorem, with (3.14) and (2.19b), we obtain a weak formulation:

$$\begin{aligned}\frac{\mathrm{d}}{\mathrm{d}t}\int_{K(t)} f\Psi\,\mathrm{d}\boldsymbol{x} &= \int_{K(t)} \partial_t(f\Psi)\,\mathrm{d}\boldsymbol{x} + \int_{\partial K(t)} \frac{1}{\varepsilon}(\boldsymbol{v}\cdot\boldsymbol{n}) f\Psi\,\mathrm{d}\Gamma \\ &= \int_{K(t)} \partial_t(f\Psi)\,\mathrm{d}\boldsymbol{x} + \int_{\partial K(t)} \frac{1}{\varepsilon}(\boldsymbol{v} f\Psi)\cdot\boldsymbol{n}\,\mathrm{d}\Gamma \\ &= \int_{K(t)} \partial_t(f\Psi)\,\mathrm{d}\boldsymbol{x} + \int_{K(t)} \frac{1}{\varepsilon}\nabla_{\boldsymbol{x}}\cdot(\boldsymbol{v} f\Psi)\,\mathrm{d}\boldsymbol{x} \\ &= \int_{K(t)} (\partial_t f + \frac{1}{\varepsilon}\boldsymbol{v}\cdot\nabla_{\boldsymbol{x}} f)\Psi + (\partial_t\Psi + \frac{1}{\varepsilon}\boldsymbol{v}\cdot\nabla_{\boldsymbol{x}}\Psi) f\,\mathrm{d}\boldsymbol{x} \\ &= \int_{K(t)} \frac{1}{\varepsilon^2}(\rho - f)\Psi\,\mathrm{d}\boldsymbol{x}.\end{aligned} \tag{3.17}$$

Inside the time interval $[t^n, t^{n+1}]$, the last equality of (3.17) can be written in an integral form:

$$\int_{K^{n+1}} f^{n+1}\Psi^{n+1}\mathrm{d}\boldsymbol{x} = \int_{K^n} f^n\Psi^n\mathrm{d}\boldsymbol{x} + \int_{t^n}^{t^{n+1}}\int_{K(t)} \frac{1}{\varepsilon^2}(\rho - f)\Psi\,\mathrm{d}\boldsymbol{x}. \tag{3.18}$$

For the integral equation (3.18), in order to avoid the strong stiffness from the source term, we can take an implicit time discretization for the source term. For a first-order approximation, a backward Euler scheme is used. For a second-order approximation, a trapezoidal quadrature rule is applied. In space, we follow the standard DG discretizations. As a result, the first-order and second-order SL DG schemes for (3.18) are defined as follows. Given $f_h^n \in V_h^k$ and $\rho_h^k \in U_h^k$, we look for $f_h^{n+1} \in V_h^k$, such that for all $K \in \mathcal{T}_h$ and $\psi \in U_h^k$,

- **First-order backward SL DG scheme:**

$$(f_h^{n+1}, \psi)_K = \frac{\varepsilon^2}{\varepsilon^2 + \Delta t} a_K(f_h^n, \psi; \boldsymbol{v}) + \frac{\Delta t}{\varepsilon^2 + \Delta t}(\rho_h^{n+1}, \psi)_K; \tag{3.19}$$

- **Second-order Crank-Nicolson SL DG scheme:**

$$(f_h^{n+1}, \psi)_K = \frac{\varepsilon^2}{2\varepsilon^2 + \Delta t} a_K(f_h^n, \psi; \boldsymbol{v}) + \frac{\Delta t}{2\varepsilon^2 + \Delta t}(\rho_h^{n+1}, \psi)_K - \frac{\Delta t}{2\varepsilon^2 + \Delta t} a_K(f_h^n - \rho_h^n, \psi; \boldsymbol{v}). \tag{3.20}$$

Here the bilinear form $a_K(f, \psi; \boldsymbol{v})$, which depends on the velocity $\boldsymbol{v}$, is defined as:

$$a_K(f, \psi; \boldsymbol{v}) = \int_{K^*} f(\boldsymbol{x}^*)\psi(\boldsymbol{x}^* + \boldsymbol{v}\Delta t/\varepsilon)\mathrm{d}\boldsymbol{x}^* = \int_K f(\boldsymbol{x} - \boldsymbol{v}\Delta t/\varepsilon)\psi(\boldsymbol{x})\mathrm{d}\boldsymbol{x} = \int_K S_{\boldsymbol{v}}^n[f]\psi\,\mathrm{d}\boldsymbol{x}. \tag{3.21}$$

We note that for second order, we take a Crank-Nicolson scheme, rather than a second order multi-step scheme as in (3.13) for ρ. The idea is to avoid the characteristic tracking across two time levels which may make the computation of $a_K(f, \psi; \boldsymbol{v})$ in (3.21) more complicated and more costly.

3.3. An oscillation-free damping approach

We now address the issue of numerical oscillations that may arise when high-order methods are applied to non-smooth problems. To control spurious oscillations for implicit methods, we adopt the damping technique [43,44] specifically for the f equations. Note that we do not apply a damping approach to the ρ equation, because at each step the real density ρ will be determined by averaging f in velocity, see the next section for more details. This damping is to suppress high-order moments of a DG scheme in a local way by using a coefficient depending on the smoothness of the solution. However the zeroth moment is not affected so that mass conservation is preserved. In our method, let us replace f with $f_h \in V_h^k$ in (3.17), a semi-discrete scheme which includes the damping term is defined as follows,

$$\frac{\mathrm{d}}{\mathrm{d}t}\int_{K(t)} f_h\Psi\mathrm{d}\boldsymbol{x} = \int_{K(t)} \frac{1}{\varepsilon^2}(\rho_h - f_h)\Psi\mathrm{d}\boldsymbol{x} - \sum_{\ell=0}^{k} \frac{\sigma_K^\ell(t)}{h_K}\int_{K(t)} (f_h - \pi_h^{\ell-1} f_h)\Psi\mathrm{d}\boldsymbol{x}, \tag{3.22}$$

where π_h^ℓ ($\ell \geq 0$) is a standard $L^2(\Omega_{\boldsymbol{x}})$ projection onto V_h^ℓ, that is, for any function w, $\pi_h^\ell w \in V_h^\ell$ satisfies

$$\int_K (\pi_h^\ell w - w) v_h \mathrm{d}\boldsymbol{x} = 0, \quad \forall v_h \in \mathcal{P}^\ell(K). \tag{3.23}$$

We also define $\pi_h^{-1} = \pi_h^0$. The damping coefficient is defined as

$$\sigma_K^\ell(t) = \frac{2(2l+1)}{2k-1} \frac{h^\ell}{\ell!} \sum_{|\boldsymbol{\alpha}|=\ell} \left(\frac{1}{N_e} [\![\partial^{\boldsymbol{\alpha}} f_h(t)]\!]^2 \right)^{\frac{1}{2}}. \tag{3.24}$$

In implementation, we take the damping term at the time level t^{n+1} but approximate $\sigma_K^\ell(t)$ using the information at the previous time level t^n. In this case, the damping term is linear with respect to the unknown f_h while the temporal accuracy is still kept due to the projection as shown in (3.23). In what follows, we denote $\sigma_K^{\ell,n} = \sigma_K^\ell(t^n)$ for simplicity.

We take the second-order SL DG scheme (3.20) in the modal form as an example here. Assume that $\{\psi_\ell(\boldsymbol{x})\}_{\ell=0}^k \subset \mathcal{P}^k(K)$ is a set of orthonormal basis functions such that

$$\int_K \psi_\ell(\boldsymbol{x}) \psi_m(\boldsymbol{x}) \mathrm{d}\boldsymbol{x} = \delta_{\ell m}, \quad \text{for all } 0 \le \ell, m \le k, \tag{3.25}$$

where $\delta_{\ell m}$ is the Kronecker delta. For $\boldsymbol{x} \in K$, we have

$$f_h^n(\boldsymbol{x}) = \sum_{\ell=0}^k f_\ell^n \psi_\ell(\boldsymbol{x}), \quad \rho_h^n(\boldsymbol{x}) = \sum_{\ell=0}^k \rho_\ell^n \psi_\ell(\boldsymbol{x}). \tag{3.26}$$

Substitute (3.26) into (3.20), we obtain that

$$f_m^{n+1} = \frac{\varepsilon^2 a_{m,1}^n + \Delta t \rho_m^{n+1} - \Delta t a_{m,2}^n}{2\varepsilon^2 + \Delta t} - \frac{2\varepsilon^2 \Delta t}{2\varepsilon^2 + \Delta t} \sum_{\ell=0}^k \frac{\sigma_K^{\ell,n}}{h_K} \sum_{j=\max(1,\ell)}^k f_j^{n+1} \delta_{jm}, \tag{3.27}$$

where $a_{m,1}^n$, $a_{m,2}^n$ correspond to the two $a_K(\cdot,\cdot)$ terms in (3.21). The first term on the right-hand side of (3.27) represents the original scheme, while the second term is the damping term. As we observe when $m = 0$, the damping term is zero, so the 0-th moment is unchanged compared to the original scheme. Namely, the mass conservation is not affected. When $m \ge 1$, we have

$$\begin{aligned} \sum_{\ell=0}^k \frac{\sigma_K^{\ell,n}}{h_K} \sum_{\max(1,\ell)} f_j^{n+1} \delta_{jm} &= \frac{\sigma_K^{0,n}}{h_K} f_m^{n+1} + \sum_{\ell=1}^k \sum_{j=\ell}^k \frac{\sigma_K^{\ell,n}}{h_K} f_j^{n+1} \delta_{jm} \\ &= \frac{\sigma_K^{0,n}}{h_K} f_m^{n+1} + \sum_{j=1}^k \sum_{\ell=1}^j \frac{\sigma_K^{\ell,n}}{h_K} f_j^{n+1} \delta_{jm} = \sum_{\ell=0}^m \frac{\sigma_K^{\ell,n}}{h_K} f_m^{n+1}. \end{aligned} \tag{3.28}$$

Let $b_0^n = 0$ and $b_m^n = \sum_{\ell=0}^m \frac{\sigma_K^{\ell,n}}{h_K}$ for $1 \le m \le k$, we obtain the updating formula for f_m^{n+1},

$$f_m^{n+1} = \frac{\varepsilon^2 a_{m,1}^n + \Delta t \rho_m^{n+1} - \Delta t a_{m,2}^n}{2\varepsilon^2 + (1 + 2\varepsilon^2 b_m^n)\Delta t}, \quad \forall\, 0 \le m \le k. \tag{3.29}$$

As we can see, the damping term is linear with respect to the unknown f_m^{n+1}, so that it is very convenient for implicit schemes, as compared to TVB limiters in [27]. Besides, it does not bring too much computational cost as compared to the original scheme. Numerical tests in Section 5 show that this damping approach can properly control numerical oscillations.

3.4. Overall algorithm

We now summarize the overall algorithm by collecting all the above proposed ingredients. We name our method SL-LDG-p-q ($p \le 2$), representing a p-th order temporal approximation and a q-th order spatial approximation. If $p = q$, we take SL-LDG-p for short. In velocity, we will apply the discrete velocity method [49]. Let $\{\boldsymbol{v}_\alpha\}_{\alpha=1}^{N_v}$ denote a set of quadrature points in $\Omega_{\boldsymbol{v}}$ and $\{w_\alpha\}_{\alpha=1}^{N_v}$ be the corresponding quadrature weights, where $N_{\boldsymbol{v}}$ is the number of quadrature points. An integral in velocity is approximated by

$$\langle f(\boldsymbol{v}) \rangle = \int_{\Omega_{\boldsymbol{v}}} f(\boldsymbol{v}) \mathrm{d}\mu \approx \sum_{\alpha=1}^{N_v} w_\alpha f(\boldsymbol{v}_\alpha). \tag{3.30}$$

To simplify the algorithm description in the following, we keep the notation $\langle \cdot \rangle$ but use the above approximation of integral in velocity in practice. Additionally, in order to improve the robustness, inspired from [22,45], we will enforce $\langle g \rangle = 0$ by introducing a predictor-corrector procedure.

The SL-LDG-1-q method is described as follows. Let $k = q - 1$. At $t = 0$, the numerical solutions are initialized via projections:

$$f_h^0(\boldsymbol{x}, \boldsymbol{v}) = \pi_h^k(f^0), \quad \rho_h^0(\boldsymbol{x}) = \left\langle f_h^0(\boldsymbol{x}, \boldsymbol{v}) \right\rangle, \quad g_h^0(\boldsymbol{x}, \boldsymbol{v}) = (f_h^0(\boldsymbol{x}, \boldsymbol{v}) - \rho_h^0(\boldsymbol{x}))/\varepsilon. \tag{3.31}$$

At time level t^n, we look for $f_h^{n+1} \in V_h^k$, $\rho_h^{n+1} \in U_h^k$, such that for any $K \in \mathcal{T}_h$, $\varphi, \phi, \gamma \in U_h^k$, $\psi, \zeta \in V_h^k$,

$$(\tilde{\boldsymbol{q}}_h^{n+1}, \varphi)_K = D\, r_K(\tilde{\rho}_h^{n+1}, \varphi), \tag{3.32a}$$

$$\left(\frac{\tilde{\rho}_h^{n+1} - \rho_h^n}{\Delta t}, \phi\right)_K + e^{-\Delta t/\varepsilon^2}\, b_K(\left\langle \boldsymbol{v} S_{\boldsymbol{v}}^n[g_h] \right\rangle, \phi) = (1 - e^{-\Delta t/\varepsilon^2})\, l_K(\tilde{\boldsymbol{q}}_h^{n+1}, \phi), \tag{3.32b}$$

$$(f_h^{n+1}, \psi)_K = \frac{\varepsilon^2}{\varepsilon^2 + \Delta t} a_K(f_h^n, \psi; \boldsymbol{v}) + \frac{\Delta t}{\varepsilon^2 + \Delta t}(\tilde{\rho}_h^{n+1}, \psi)_K, \tag{3.32c}$$

$$(\rho_h^{n+1}, \gamma)_K = \left(\left\langle f_h^{n+1} \right\rangle, \gamma\right)_K, \tag{3.32d}$$

$$(g_h^{n+1}, \zeta)_K = ((f_h^{n+1} - \rho_h^{n+1})/\varepsilon, \zeta)_K. \tag{3.32e}$$

The bilinear forms are provided in (3.10) in Section 3.1 and (3.21) in Section 3.2. The temporary variable g_h^n introduced here can be manually eliminated using (3.32e). To implement this method, we first substitute (3.32a) into (3.32b) to form a low-dimensional (space-only) sparse linear algebraic system. By solving such a system, we get a macroscopic prediction $\tilde{\rho}_h^{n+1}$ at time level t^{n+1}. Based on this, the high-dimensional unknowns f_h^{n+1} at all discrete velocities are completely decoupled. Thereby we are able to efficiently compute f_h^{n+1} by (3.32c) via parallel computing. We finish the algorithm by correcting the macroscopic and microscopic unknowns ρ_h^{n+1}, g_h^{n+1} at t^{n+1} using projections (3.32d) and (3.32e) to keep an exact conservation of mass.

The SL-LDG-2-q method is almost the same. At time level t^n, we look for $f_h^{n+1} \in V_h^k$, $\rho_h^{n+1} \in U_h^k$, such that for all $K \in \mathcal{T}_h$, $\varphi, \phi, \gamma \in U_h^k$, $\psi, \zeta \in V_h^k$,

$$(\tilde{\boldsymbol{q}}_h^{n+1}, \varphi)_K = D\, r_K(\tilde{\rho}_h^{n+1}, \varphi), \tag{3.33a}$$

$$\left(\frac{3\tilde{\rho}_h^{n+1} - 4\rho_h^n + \rho_h^{n-1}}{2\Delta t}, \phi\right)_K + e^{-\Delta t/\varepsilon^2}\, b_K(\left\langle \boldsymbol{v} S_{\boldsymbol{v}}^n[g_h] \right\rangle, \phi) = (1 - e^{-\Delta t/\varepsilon^2})\, l_K(\tilde{\boldsymbol{q}}_h^{n+1}, \phi), \tag{3.33b}$$

$$(f_h^{n+1}, \psi)_K = \frac{\varepsilon^2}{2\varepsilon^2 + \Delta t} a_K(f_h^n, \psi; \boldsymbol{v}) + \frac{\Delta t}{2\varepsilon^2 + \Delta t}(\tilde{\rho}_h^{n+1}, \psi)_K - \frac{\Delta t}{2\varepsilon^2 + \Delta t} a_K((f_h^n - \rho_h^n), \psi; \boldsymbol{v}), \tag{3.33c}$$

$$(\rho_h^{n+1}, \gamma)_K = \left(\left\langle f_h^{n+1} \right\rangle, \gamma\right)_K, \tag{3.33d}$$

$$(g_h^{n+1}, \zeta)_K = ((f_h^{n+1} - \rho_h^{n+1})/\varepsilon, \zeta)_K. \tag{3.33e}$$

To start this multi-step solver, we could apply the SL-LDG-1-q method (3.32) for $n = 0$ and then run with (3.33) for $n \geq 1$.

Remark 3.1. To implement the proposed method, we have to evaluate four types of integrals:

(a) $\int_K u(\boldsymbol{x}) v(\boldsymbol{x}) \mathrm{d}\boldsymbol{x}$, e.g., volume integrals in $r_K(\cdot,\cdot)$, $l_K(\cdot,\cdot)$;
(b) $\int_{\partial K} u(\boldsymbol{x}) v(\boldsymbol{x}) \mathrm{d}\boldsymbol{x}$, e.g., flux integrals in $r_K(\cdot,\cdot)$, $l_K(\cdot,\cdot)$;
(c) $\int_K u(\boldsymbol{x} - a\boldsymbol{y}) v(\boldsymbol{x}) \mathrm{d}\boldsymbol{x}$, e.g., volume integrals in $a_K(\cdot,\cdot;\boldsymbol{v})$, $b_K(\cdot,\cdot)$;
(d) $\int_{\partial K} u(\boldsymbol{x} - a\boldsymbol{y}) v(\boldsymbol{x}) \mathrm{d}\boldsymbol{x}$, e.g., flux integrals in $b_K(\cdot,\cdot)$.

For simplicity, we assume that K is rectangular. To evaluate (a) and (b), we can simply apply a Gauss-Legendre quadrature. However, evaluating integrals (c) and (d) is more challenging as $u(\boldsymbol{x} - a\boldsymbol{y})$ might cross elements. Our approach for handling integrals (c) and (d) comprises three steps: (1) tracking elements along characteristic lines, (2) clipping upstream elements with background elements, and (3) collocating quadrature points at the intersection region. Thanks to constant velocities, upstream elements are rectangular. Let us take a 2D uniform mesh as an example. As depicted in Fig. 3.1, an element K can be clipped into four small sub-elements $\{K_\alpha\}_{\alpha=1}^4$, ensuring continuity of $u(\boldsymbol{x} - a\boldsymbol{y})$ within each sub-element. To evaluate integrals of type (c), we assign 2D Gauss-Legendre points (black crosses) to each subregion and compute them as follows:

$$\int_K u(\boldsymbol{x} - a\boldsymbol{y}) v(\boldsymbol{x}) \mathrm{d}\boldsymbol{x} = \sum_\alpha \int_{K_\alpha} u(\boldsymbol{x} - a\boldsymbol{y}) v(\boldsymbol{x}) \mathrm{d}\boldsymbol{x} \approx \sum_{\alpha,\beta} w_\beta u(\boldsymbol{x}_{\alpha,\beta}^*) v(\boldsymbol{x}_{\alpha,\beta}), \tag{3.34}$$

where $\boldsymbol{x}_{\alpha,\beta}^*$ corresponds to the black cross on the left and $\boldsymbol{x}_{\alpha,\beta}$ on the right. Similarly, for each interface ∂K (or ∂K^*), we apply a 1D Gauss-Legendre quadrature (blue stars) to compute line integrals of type (d). It is worth noting that the key aspect of the clipping algorithm for a hyperrectangle is locating points of intersection within an element, namely, the central red circles in Fig. 3.1. As we can see here, with constant velocities, clipping can be achieved using 1D algorithms through dimensional splitting, which makes it easy to extend our method to 3D cases.

Remark 3.2. Here we briefly discuss the boundary treatment; for more details, we refer to [12,13,23]. By using an SL method, we track a point from $(t, \boldsymbol{x})$ to $(t_*, \boldsymbol{x}_*)$. When the point $\boldsymbol{x}_*$ exceeds the computational domain $\Omega_{\boldsymbol{x}}$, we need to assign ghost values for $f(t_*, \boldsymbol{x}_*, \boldsymbol{v})$ and $\rho(t_*, \boldsymbol{x}_*)$. Taking the 1D case as an example, we focus on the left boundary. For a periodic boundary condition, let P be a periodic mapping that maps a ghost point x_* to an interior point $P(x_*)$, as shown in Fig. 3.2(a). We simply set

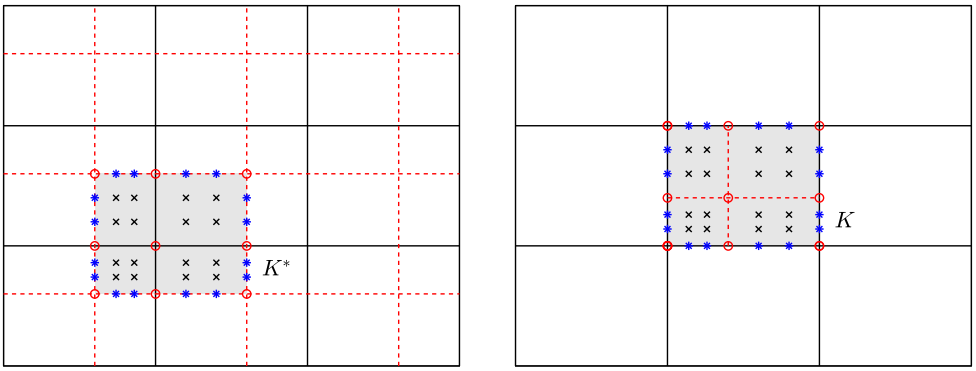

Fig. 3.1. Illustration of quadrature points for convolution integrals: Lagrangian element K^* (left); Eulerian element K (right). The black solid lines represent Eulerian mesh, while the red dashed lines represent Lagrangian mesh. The red circles determine the geometric partitions. The black crosses denote the Gauss-Legendre points for the volume integral of type (c), while the blue stars are used for the flux integral of type (d). (For interpretation of the colors in the figure(s), the reader is referred to the web version of this article.)

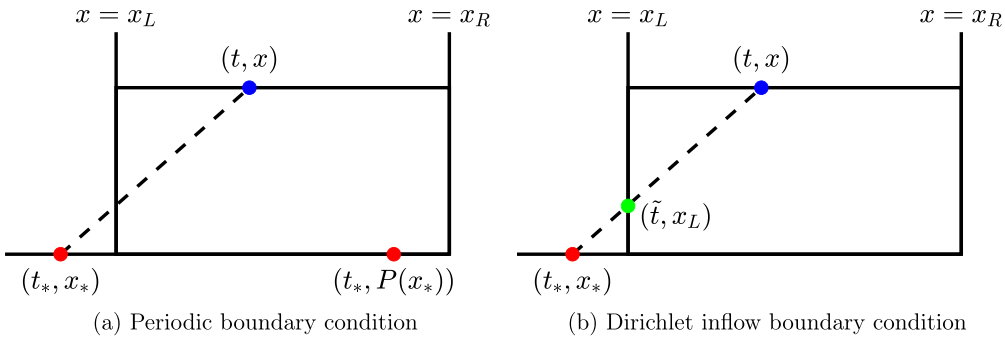

Fig. 3.2. Graphic description of boundary treatment for exterior points.

$$f(t_*, x_*, v) = f(t_*, P(x_*), v) \quad \text{and} \quad \rho(t_*, x_*) = \rho(t_*, P(x_*)). \tag{3.35}$$

For a Dirichlet inflow boundary condition, the characteristics would intersect with the left boundary at $(\tilde{t}, x_L)$ as shown in Fig. 3.2(b). In this case, we take a first-order approximation by using the values at (t_*, x_L) to approximate the values at $(\tilde{t}, x_L)$, that is

$$f(t_*, x_*, v) = f_L(\tilde{t}, v) \approx f_L(t_*, v) \quad \text{and} \quad \rho(t_*, x_*) = \rho_L(\tilde{t}) \approx \rho_L(t_*). \tag{3.36}$$

We note that $\rho_L(t_*)$ is obtained by using a close-loop boundary condition as detailed in [12,13,23,27].

4. Theoretical analysis

In this section, we first analyze the AP property of the proposed SL-LDG-p-q methods by using the simple linear telegraph equation (2.1a). Then we conduct a Fourier analysis to study their stability as in [27].

4.1. Formal asymptotic analysis

Theorem 4.1. *Assume that the telegraph equation (1.1)(2.1a) is equipped with a periodic boundary condition and a well-prepared initial condition. For a fixed time step Δt and mesh size h, as $\varepsilon \to 0$, the SL-LDG-p-q methods ($p = 1, 2$, $q \geq 1$) are formally AP.*

Proof. We only consider the SL-LDG-1-q method for the telegraph equation. The proof of the SL-LDG-2-q method is almost the same. Let $\varepsilon \to 0$, (3.32) formally becomes

$$\begin{aligned}
&(q_h^{n+1}, \varphi)_K = r_K(\tilde{\rho}_h^{n+1}, \varphi), \quad \forall \varphi \in U_h^k;\\
&(\frac{\tilde{\rho}_h^{n+1} - \rho_h^n}{\Delta t}, \phi)_K = l_K(q_h^{n+1}, \phi), \quad \forall \phi \in U_h^k;\\
&(f_h^{n+1}, \psi)_K = (\tilde{\rho}_h^{n+1}, \psi)_K, \quad \forall \psi \in V_h^k;\\
&(\rho_h^{n+1}, \gamma)_K = (\langle f_h^{n+1} \rangle, \gamma), \quad \forall \gamma \in V_h^k.
\end{aligned}$$

This implies $\rho_h^{n+1} = \langle f_h^{n+1} \rangle = f_h^{n+1} = \tilde{\rho}_h^{n+1}$, where $\tilde{\rho}_h^{n+1}$ satisfies a backward Euler LDG scheme for the limiting heat equation. □

4.2. Fourier stability analysis

Here we carry out a Fourier analysis in the one-dimensional case. We employ a periodic boundary condition and a uniform mesh with cells $I_i = [x_{i-\frac{1}{2}}, x_{i+\frac{1}{2}}]$ for $1 \le i \le N$. Besides, we consider the SL-LDG-p-q methods with $p = 1, 2$, $q \ge 1$ and the left-right alternating flux pair, applied to the telegraph equation where $\Omega_v = \{-1, 1\}$. Let the numerical solutions be

$$\rho_h^n(x) = \sum_{l=0}^{q-1} \rho_{i,l}^n \phi_i^l(x), \quad q_h^n(x) = \sum_{l=0}^{q-1} q_{i,l}^n \phi_i^l(x), \quad f_h^n(x, v_\alpha) = \sum_{l=0}^{q-1} f_{i,l,\alpha}^n \phi_i^l(x), \quad \forall x \in I_i, \tag{4.1}$$

where $v_\alpha = -1, 1$, $\phi_i^l(x) = \phi^l(\xi_i)$ with $\xi_i = \frac{x - x_i}{h_i}$ and ϕ^l is the l-th scaled Legendre polynomial on $[-\frac{1}{2}, \frac{1}{2}]$,

$$\phi^0(\xi) = 1, \quad \phi^1(\xi) = \xi, \quad \phi^2(\xi) = \xi^2 - \frac{1}{12}, \quad \ldots. \tag{4.2}$$

We collect unknowns as vectors $\boldsymbol{\rho}_i^n = (\rho_{i,0}^n, \ldots, \rho_{i,q-1}^n)^T$, $\boldsymbol{f}_{i,\alpha}^n = (f_{i,0,\alpha}^n, \ldots, f_{i,q-1,\alpha}^n)^T$ and take the ansatz $\boldsymbol{\rho}_i^n = \hat{\boldsymbol{\rho}}^n \exp(\mathcal{I}\kappa x_i)$, $\boldsymbol{f}_{i,\alpha}^n = \hat{\boldsymbol{f}}_\alpha^n \exp(\mathcal{I}\kappa x_i)$ with the imaginary unit $\mathcal{I}^2 = -1$, $\alpha = 1, \ldots, N_v$. Note that the auxiliary variable q_h^n can be eliminated. Denoting

$$\boldsymbol{U}_1^n = (\hat{\boldsymbol{\rho}}^n, \hat{\boldsymbol{f}}_1^n, \ldots, \hat{\boldsymbol{f}}_{N_v}^n, \hat{\boldsymbol{\rho}}^n)^T, \quad \boldsymbol{U}_2^n = (\hat{\boldsymbol{\rho}}^n, \hat{\boldsymbol{f}}_1^n, \ldots, \hat{\boldsymbol{f}}_{N_v}^n, \hat{\boldsymbol{\rho}}^n, \hat{\boldsymbol{\rho}}^{n-1})^T,$$

the SL-LDG-p-q methods for telegraph equation can be written as

$$\boldsymbol{U}_p^{n+1} = \boldsymbol{A}^{p,q}(\varepsilon, h, \Delta t; \omega) \boldsymbol{U}_p^n, \tag{4.3}$$

where $\boldsymbol{A}^{p,q}$ is the amplification matrix depending on the model parameter ε, mesh size h, time step size Δt, and the discrete wave number $\omega = \kappa h \in [0, 2\pi]$. Theorem 4.2 illustrates the structure of the amplification matrix $\boldsymbol{A}^{p,q}$, with its proof presented in the appendix.

Theorem 4.2. *For any given $q \ge 1$ and $p = 1, 2$, the amplification matrix $\boldsymbol{A}^{p,q}$ related to SL-LDG-p-q method depends only on the terms $\frac{\varepsilon}{h}$ and $\frac{\Delta t}{\varepsilon h}$, namely, $\boldsymbol{A}^{p,q} = \boldsymbol{A}^{p,q}(\frac{\varepsilon}{h}, \frac{\Delta t}{\varepsilon h}; \omega)$.*

Next, we use the following principle to characterize the non-increasing L^2 energy stability.

Principle for Numerical Stability [23]. For any given $\varepsilon, h, \Delta t$, let the eigenvalues of $\boldsymbol{A}$ be $\lambda_i(\omega)$, $i = 1, \ldots, N$. Our scheme is "stable", if for all $\omega \in [0, 2\pi]$, it satisfies either

$$\max_{i=1,\ldots,N} \left\{ \left| \lambda_i(\omega) \right| \right\} < 1, \quad \text{or} \tag{4.4a}$$

$$\max_{i=1,\ldots,N} \left\{ \left| \lambda_i(\omega) \right| \right\} = 1 \quad \text{and} \quad \boldsymbol{A} \text{ is diagonalizable.} \tag{4.4b}$$

We verify the uniformly unconditional stability of the proposed schemes from numerical sampling. Motivated by Theorem 4.2, we define $\sigma = \log_{10}(\varepsilon/h)$ and $\eta = \log_{10}(\varepsilon^2/\Delta t)$. Subsequently, we uniformly sample σ using 1000 points within $[-5, 5]$, and η with 800 points inside $[-4, 4]$. Additionally, we sample the discrete wave number ω uniformly within $[0, 2\pi]$ using 500 points. Based on the above stability principle, the SL-LDG-p-q methods with $p = 1, 2$ and $q = 1, 2$ are verified to be uniformly unconditionally stable.

5. Numerical results

In this section, we present a set of numerical tests to demonstrate the performance of the proposed first-order and second-order SL-LDG-p ($p = 1, 2$) methods in terms of their accuracy, stability and efficiency, when applied to the multiscale problem (1.1) with either smooth or non-smooth solutions. For the second-order scheme, when applied to non-smooth problems, the oscillation-free damping limiter is used, and we denote the scheme as SL-LDG-2-D. The spatial domain is taken as $\Omega_{\boldsymbol{x}} = [a, b]^d$, with d being the dimension in space. For simplicity, a uniform spatial mesh with N^d elements is used and the mesh size is $h = (b-a)/N$. We apply the boundary treatment described in Remark 3.2. We take a time step $\Delta t = Ch$ where C is a referred CFL number, which is independent of the Knudsen number ε and mesh size h, but would be specific to each problem. By using an SL method with DG discretization for the convection part, the scheme is even more efficient than the finite difference scheme in [27]. Besides, we will show that the scheme is highly parallel, especially for high-dimensional problems (3D in $\boldsymbol{x}$ and 2D in $\boldsymbol{v}$).

5.1. One-dimensional transport problem

In this subsection, we consider 1D transport problems. We start with two-velocity models (2.1a)-(2.1b), and then turn to the one-group transport equation in a slab geometry (2.2) in the case $d = 1$. For each collision operator, the corresponding approximation model has been shown in [27].

Table 5.1
Accuracy test for the telegraph equation (Section 5.1.1). Numerical errors and convergence orders of the SL-LDG-1 method in L^1 and L^∞ norms. $T = 1$.

Parameters		$\Delta t = 0.5\Delta x$				$\Delta t = 5.0\Delta x$			
ε	N	$E^\rho_{N,1}$	$O^\rho_{N,1}$	$E^\rho_{N,\infty}$	$O^\rho_{N,\infty}$	$E^\rho_{N,1}$	$O^\rho_{N,1}$	$E^\rho_{N,\infty}$	$O^\rho_{N,\infty}$
0.5	80	1.59E-02	-	4.48E-03	-	1.38E-01	-	3.46E-02	-
	160	7.61E-03	1.06	2.18E-03	1.04	8.01E-02	0.79	2.00E-02	0.79
	320	3.73E-03	1.03	1.08E-03	1.02	3.51E-02	1.19	8.80E-03	1.19
	640	1.85E-03	1.01	5.35E-04	1.01	1.42E-02	1.31	3.55E-03	1.31
10^{-1}	80	1.43E-02	-	4.68E-03	-	6.05E-02	-	1.54E-02	-
	160	9.11E-03	0.65	2.86E-03	0.71	3.72E-02	0.70	9.43E-03	0.71
	320	4.96E-03	0.88	1.63E-03	0.81	2.10E-02	0.83	5.30E-03	0.83
	640	2.37E-03	1.07	8.59E-04	0.93	1.30E-02	0.69	3.28E-03	0.69
10^{-2}	80	1.08E-02	-	4.05E-03	-	5.75E-02	-	1.47E-02	-
	160	5.39E-03	1.00	2.02E-03	1.00	3.32E-02	0.79	8.44E-03	0.80
	320	2.70E-03	1.00	1.01E-03	1.00	1.73E-02	0.94	4.38E-03	0.95
	640	1.36E-03	0.99	5.07E-04	1.00	8.85E-03	0.96	2.24E-03	0.97
10^{-6}	80	1.07E-02	-	4.05E-03	-	5.75E-02	-	1.47E-02	-
	160	5.36E-03	1.00	2.02E-03	1.00	3.32E-02	0.79	8.43E-03	0.80
	320	2.68E-03	1.00	1.01E-03	1.00	1.72E-02	0.94	4.37E-03	0.95
	640	1.34E-03	1.00	5.02E-04	1.00	8.81E-03	0.97	2.23E-03	0.97

5.1.1. *Telegraph equation*

To evaluate the performance of the proposed methods for the telegraph equation (2.1a), we present two representative tests here.

Case 1: Accuracy test. Consider the following smooth, exact solution

$$f(t,x,v) = \frac{1}{4}\left[-\frac{1}{\gamma}e^{-\gamma t}\sin(x) + v\varepsilon e^{-\gamma t}\cos(x)\right] + \frac{1}{2}, \quad \gamma = \frac{2}{1+\sqrt{1-4\varepsilon^2}} \tag{5.1}$$

on $\Omega_x = [-\pi, \pi]$ with a periodic boundary condition. The numerical errors for the macroscopic density ρ in a L^r-norm and corresponding convergence orders at a final time T are defined as

$$E^\rho_{N,r} = \|\rho_h(T,x) - \rho(T,x)\|_{L^r}, \quad O^\rho_{N,r} = \log_2(E^\rho_{N,r}/E^\rho_{2N,r}), \tag{5.2}$$

for $r = 1, \infty$ respectively. We take $T = 1$ in this example. In Tables 5.1 and 5.2, we observe the desired convergence orders and uniform stability of p-th ($p = 1, 2$) order schemes in both kinetic and diffusive regimes. An order reduction occurs when $\varepsilon = \mathcal{O}(\sqrt{\Delta t})$, especially for the second-order scheme, which coincides with the theoretical results in Theorem 2.2 and numerical results of the finite difference scheme in [27].

Case 2: Square wave. Given a discontinuous square-shaped initial data from [12]:

$$f(x,v,0) = 1 - \mathcal{H}(|x| - 0.2), \quad x \in [-1,1] \tag{5.3}$$

with a Dirichlet boundary condition, where $\mathcal{H}(x)$ is the Heaviside function, we will show the effectiveness of the oscillation-free limiter with a damping in controlling numerical oscillations. In Fig. 5.1, we show the numerical solutions at time $T = 0.5$ for $\varepsilon = 1.0$ and $T = 0.05$ for $\varepsilon = 10^{-6}$. We take a fairly large time step $\Delta t = 1.5\Delta x$ with $h = 0.025$. In the kinetic regime, the original SL-LDG-2 scheme exhibits clear spurious numerical oscillations, which can be significantly reduced by adding the damping term. Besides, the proposed methods are shown to be AP and stable with a large time step in the diffusive regime $\varepsilon = 10^{-6}$.

5.1.2. *Advection-diffusion equation*

We now turn to the model with the collision operator (2.1b), which converges to an advection-diffusion equation as $\varepsilon \to 0$. Similarly, two cases are considered.

Case 1: Accuracy test in the diffusive regime. Let $A = 1$ and $\Omega_x = [-\pi, \pi]$, consider the following exact solution

$$f(t,x,v) = e^{-t}\sin(x-t) + \varepsilon v e^{-t}(\sin(x-t) - \cos(x-t)), \quad \rho(t,x) = e^{-t}\sin(x-t) \tag{5.4}$$

and a periodic boundary condition. We carry out a convergence study at $T = 1$ and $\varepsilon = 10^{-6}$. Table 5.3 shows the desired convergence behaviors of the first- and second-order schemes under small and large time steps.

Case 2: Riemann problem. The Riemann initial data is given as

$$f(0,x,v) = f_R\mathcal{H}(x) + f_L(1 - \mathcal{H}(x)), \quad f_R = 2.0, \quad f_L = 4.0 \tag{5.5}$$

Table 5.2
Accuracy test for the telegraph equation (Section 5.1.1). Numerical errors and convergence orders of the SL-LDG-2 method in L^1 and L^∞ norms. $T = 1$.

Parameters		$\Delta t = 0.5\Delta x$				$\Delta t = 5.0\Delta x$			
ε	N	$E^\rho_{N,1}$	$O^\rho_{N,1}$	$E^\rho_{N,\infty}$	$O^\rho_{N,\infty}$	$E^\rho_{N,1}$	$O^\rho_{N,1}$	$E^\rho_{N,\infty}$	$O^\rho_{N,\infty}$
0.5	80	2.37E-03	-	6.12E-04	-	1.04E-01	-	2.60E-02	-
	160	6.14E-04	1.95	1.58E-04	1.95	4.36E-02	1.25	1.09E-02	1.25
	320	1.56E-04	1.98	4.00E-05	1.98	1.34E-02	1.70	3.35E-03	1.70
	640	3.92E-05	1.99	1.01E-05	1.99	3.65E-03	1.87	9.13E-04	1.88
10^{-1}	80	4.04E-03	-	1.10E-03	-	3.49E-02	-	8.81E-03	-
	160	3.07E-03	0.40	7.91E-04	0.48	1.08E-02	1.68	2.73E-03	1.69
	320	1.53E-03	1.00	3.89E-04	1.02	5.21E-03	1.06	1.31E-03	1.06
	640	5.57E-04	1.46	1.41E-04	1.47	4.17E-03	0.32	1.04E-03	0.33
10^{-2}	80	2.81E-04	-	1.64E-04	-	3.15E-02	-	7.98E-03	-
	160	9.67E-05	1.54	4.75E-05	1.78	7.34E-03	2.10	1.86E-03	2.10
	320	5.17E-05	0.90	1.87E-05	1.34	1.66E-03	2.14	4.21E-04	2.14
	640	4.05E-05	0.35	1.16E-05	0.69	4.23E-04	1.97	1.07E-04	1.97
10^{-6}	80	2.45E-04	-	1.54E-04	-	3.15E-02	-	7.97E-03	-
	160	5.99E-05	2.03	3.83E-05	2.01	7.30E-03	2.11	1.85E-03	2.11
	320	1.49E-05	2.01	9.55E-06	2.00	1.62E-03	2.17	4.12E-04	2.17
	640	3.71E-06	2.00	2.38E-06	2.00	3.86E-04	2.07	9.79E-05	2.07

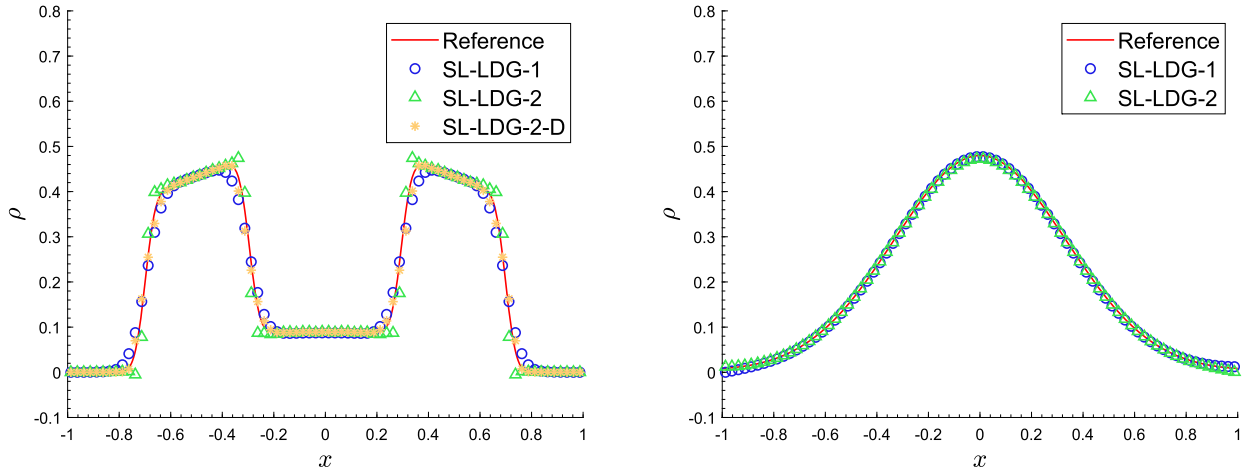

(a) kinetic regime: $\varepsilon = 1.0$, $T = 0.5$ (b) diffusive regime: $\varepsilon = 10^{-6}$, $T = 0.05$

Fig. 5.1. Square wave problem for the telegraph equation (Section 5.1.1). Density ρ of the SL-LDG-p ($p = 1, 2$) solutions at different regimes. $h = 0.025$ and $\Delta t = 1.5h$. The reference solution is computed by the first-order finite difference method based on micro-macro decomposition with $h = 0.004$ and $\Delta t = 0.001$.

with an inflow and outflow boundary condition. We set $A = 1$ and $\Omega_x = [-10, 10]$. The numerical solutions in the kinetic regime ($\varepsilon = 0.5$) and the diffusive regime ($\varepsilon = 10^{-6}$) are depicted in Fig. 5.2. Two time steps are taken: $\Delta t = 0.5h$ and $\Delta t = 2.5h$. As we can see, our proposed schemes are stable for both time steps in both regimes. However, the larger the time step is, the bigger the deviation errors are, especially in the kinetic regime. The second-order scheme performs better than the first-order scheme.

5.1.3. One-group transport equation in a slab geometry

This is a transport problem with a continuous velocity space, and we take the discrete velocity method with a 16-point Gaussian-Legendre quadrature rule on $\Omega_v = [-1, 1]$. Here, we provide two typical numerical examples.

Case 1: Accuracy test. Let $\sigma_s = 1$, $\sigma_a = 0$ and $S \equiv 0$ and consider the following smooth initial data with a periodic boundary condition:

$$f(0, x, v) = 2 + \sin(x) - \varepsilon v \cos(x), \quad x \in [-\pi, \pi]. \tag{5.6}$$

The convergence study is carried out by taking $T = 1$, $N = 40 \cdot 2^k$ and $\Delta t = T/(3 \cdot 2^k) \approx 2.12\Delta x$. Since the exact solutions of f and ρ are not available, we compute the errors by comparing two solutions on two consecutive meshes. Specifically, we define

$$RE^\rho_{N,r} = \|\rho_h(T, x) - \rho_{h/2}(T, x)\|_{L^r}, \quad RO^\rho_{N,r} = \log_2(RE^\rho_{N,r}/RE^\rho_{2N,r}), \tag{5.7}$$

Table 5.3
Accuracy test for advection-diffusion equation (Section 5.1.2). Numerical errors and convergences orders of the SL-LDG-p ($p = 1, 2$) methods in the diffusive regime $\varepsilon = 10^{-6}$.

Parameter		$\Delta t = 0.5\Delta x$				$\Delta t = 5.0\Delta x$			
p	N	$E^{\rho}_{N,1}$	$O^{\rho}_{N,1}$	$E^{\rho}_{N,\infty}$	$O^{\rho}_{N,\infty}$	$E^{\rho}_{N,1}$	$O^{\rho}_{N,1}$	$E^{\rho}_{N,\infty}$	$O^{\rho}_{N,\infty}$
1	80	8.22E-02	-	3.14E-02	-	4.49E-01	-	1.29E-01	-
	160	4.19E-02	0.97	1.59E-02	0.99	2.57E-01	0.81	7.12E-02	0.86
	320	2.12E-02	0.99	7.93E-03	1.00	1.36E-01	0.91	3.76E-02	0.92
	640	1.06E-02	0.99	3.97E-03	1.00	7.02E-02	0.95	1.93E-02	0.96
2	80	2.57E-03	-	8.81E-04	-	2.96E-01	-	7.42E-02	-
	160	6.35E-04	2.02	2.20E-04	2.00	6.71E-02	2.14	1.68E-02	2.14
	320	1.56E-04	2.03	5.46E-05	2.01	1.64E-02	2.03	4.11E-03	2.03
	640	3.92E-05	1.99	1.37E-05	2.00	3.99E-03	2.04	1.00E-03	2.04

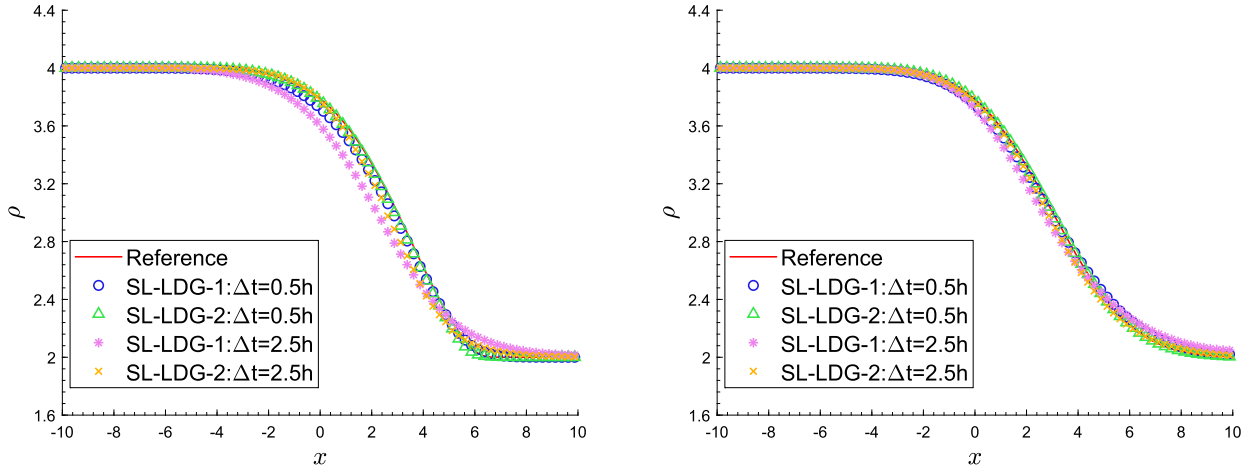

(a) kinetic regime: $\varepsilon = 0.5$, $T = 3.0$ (b) diffusive regime: $\varepsilon = 10^{-6}$, $T = 3.0$

Fig. 5.2. Riemann problem for advection-diffusion equation (Section 5.1.2). Density ρ of the SL-LDG-p ($p = 1, 2$) solutions at different regimes. $h = 0.25$. The reference solution is computed by the first-order finite difference method based on micro-macro decomposition with $h = 0.04$ and $\Delta t = 0.01$.

Table 5.4
Accuracy test for one-group transport equation (Section 5.1.3). Numerical errors and convergence orders of the SL-LDG-p ($p = 1, 2$) methods in L^1 and L^∞ norms. $T = 1$.

Parameters		$p = 1$				$p = 2$			
ε	N	$RE^{\rho}_{N,1}$	$RO^{\rho}_{N,1}$	$RE^{\rho}_{N,\infty}$	$RO^{\rho}_{N,\infty}$	$RE^{\rho}_{N,1}$	$RO^{\rho}_{N,1}$	$RE^{\rho}_{N,\infty}$	$RO^{\rho}_{N,\infty}$
0.5	80	1.32E-01	-	3.29E-02	-	2.23E-03	-	1.10E-03	-
	160	6.99E-02	0.92	1.75E-02	0.91	5.58E-04	2.00	2.69E-04	2.03
	320	3.62E-02	0.95	9.05E-03	0.95	1.40E-04	2.00	6.65E-05	2.02
	640	1.84E-02	0.97	4.61E-03	0.97	3.49E-05	2.00	1.66E-05	2.01
10^{-2}	80	1.31E-01	-	3.27E-02	-	3.44E-03	-	2.23E-03	-
	160	6.15E-02	1.09	1.54E-02	1.09	1.02E-03	1.76	6.63E-04	1.75
	320	3.00E-02	1.04	7.50E-03	1.03	2.53E-04	2.01	1.65E-04	2.00
	640	1.49E-02	1.01	3.72E-03	1.01	6.21E-05	2.02	4.08E-05	2.02
10^{-6}	80	1.41E-01	-	3.51E-02	-	4.09E-03	-	2.65E-03	-
	160	7.03E-02	1.00	1.76E-02	1.00	1.02E-03	2.00	6.64E-04	2.00
	320	3.51E-02	1.00	8.78E-03	1.00	2.55E-04	2.00	1.66E-04	2.00
	640	1.76E-02	1.00	4.39E-03	1.00	6.37E-05	2.00	4.15E-05	2.00

for $r = 1, \infty$. Table 5.4 validates the convergence order of both first- and second-order schemes from kinetic regime $\varepsilon = 0.5$ to diffusive regime $\varepsilon = 10^{-6}$.

Case 2: Boundary condition test. Given $\sigma_s = 1, \sigma_a = 0$ and $S \equiv 0$, we consider a benchmark problem from [12,10] with an isotropic Dirichlet boundary condition and zero initial data on $\Omega_x = [0, 1]$, namely,

$$f_L(t, v) = 1, \quad f_R(t, v) = 0, \quad f(0, x, v) = 0, \quad x \in \Omega_x. \tag{5.8}$$

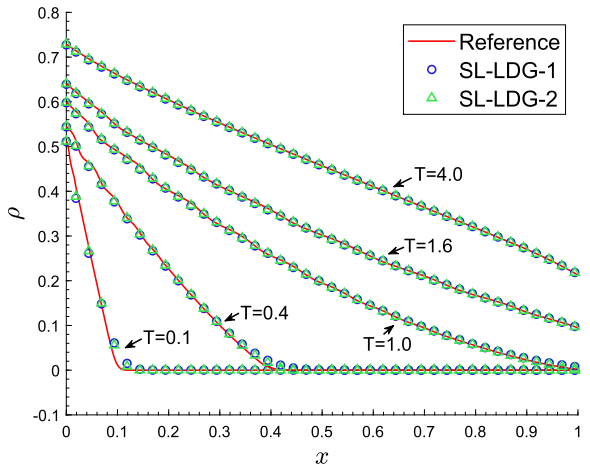

(a) kinetic regime: $\varepsilon = 1.0$, $\Delta t = 0.5h$

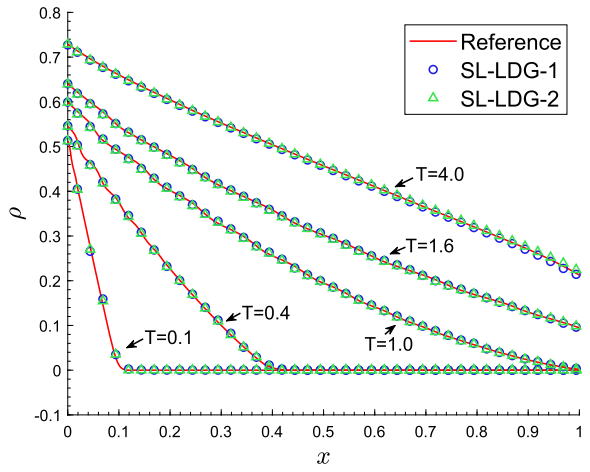

(b) kinetic regime: $\varepsilon = 1.0$, $\Delta t = 2.5h$

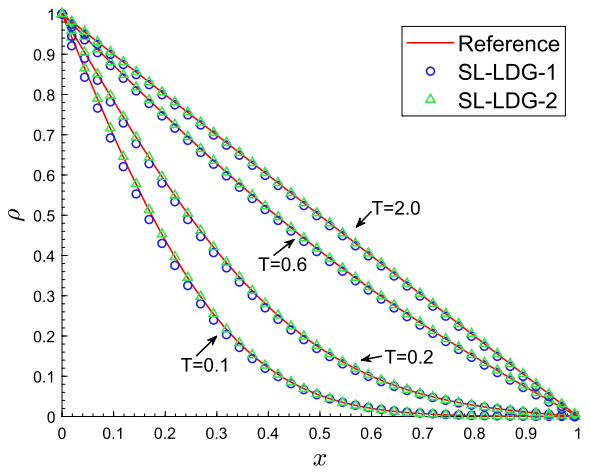

(c) diffusive regime: $\varepsilon = 10^{-6}$, $\Delta t = 0.5h$

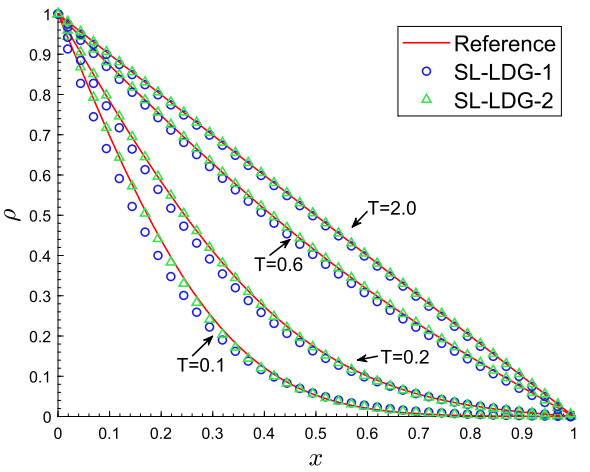

(d) diffusive regime: $\varepsilon = 10^{-6}$, $\Delta t = 2.5h$

Fig. 5.3. Isotropic Dirichlet boundary test for one-group transport equation (Section 5.1.3). Density ρ of the SL-LDG-p ($p = 1, 2$) solutions at different regimes. $h = 0.0125$. The reference solution is computed by the first-order finite difference method based on micro-macro decomposition with $h = 0.001$ and $\Delta t = 0.00025$.

The numerical results shown in Fig. 5.3 demonstrate the robustness of our proposed schemes, which are AP when it is close to the diffusive limit, have large time step stability, and are effective for such a Dirichlet boundary condition.

5.2. Multi-dimensional transport problems

Now we consider some multi-dimensional transport problems (2.5) to demonstrate the efficiency of our proposed schemes. For high-dimensional problems, the velocity is defined as vectors on a unit sphere $\Omega_{\boldsymbol{v}}$, and the average in the velocity space is defined as $\langle\cdot\rangle = \frac{1}{4\pi}\int_{\Omega_{\boldsymbol{v}}} \cdot \, \mathrm{d}\boldsymbol{v}$. For velocity discretization, we adopt the Lebedev quadrature rule with $N_{\boldsymbol{v}}$ points [50]. Periodic or zero boundary conditions are considered.

By setting σ_s, σ_a, $\sigma = \sigma_s + \varepsilon^2\sigma_a$ and following the procedure in Section 2, we can obtain a similar approximation model [27]

$$\partial_t \rho + e^{-\sigma(t-t^n)/\varepsilon^2}\nabla_{\boldsymbol{x}} \cdot \langle \boldsymbol{v} g(t^n, \boldsymbol{x}^n, \boldsymbol{v})\rangle = \nabla_{\boldsymbol{x}} \cdot \left(\frac{1}{\sigma}(1 - e^{-\sigma(t-t^n)/\varepsilon^2})\nabla_{\boldsymbol{x}}\rho\right) - \sigma_a \rho + S, \tag{5.9a}$$

$$\partial_t f + \frac{1}{\varepsilon}\boldsymbol{v}\cdot\nabla_{\boldsymbol{x}} f = \frac{\sigma_s}{\varepsilon^2}(\rho - f) - \sigma_a f + S. \tag{5.9b}$$

5.2.1. The reduced 2D problem

Firstly, we carry out an accuracy test with the exact solution from [51]:

$$f(t, x, y, v_x, v_y) = e^{-t}\sin^2(2\pi x)\sin^2(2\pi y)\left(1 + \varepsilon\left(\frac{v_y + v_y^3}{3}\right)\right), \quad (x, y) \in [0, 1]^2. \tag{5.10}$$

Table 5.5
2D Accuracy test (Section 5.2.1). Numerical errors and convergence orders of the SL-LDG-p ($p=1,2$) methods in L^1 and L^∞ norms. $T=1$.

Parameter		$p=1$				$p=2$			
ε	$N_x\times N_y$	$E^\rho_{N,1}$	$O^\rho_{N,1}$	$E^\rho_{N,\infty}$	$O^\rho_{N,\infty}$	$E^\rho_{N,1}$	$O^\rho_{N,1}$	$E^\rho_{N,\infty}$	$O^\rho_{N,\infty}$
1.0	16×16	2.68E-02	-	1.20E-01	-	1.26E-02	-	4.98E-02	-
	32×32	1.42E-02	0.92	6.20E-02	0.95	3.21E-03	1.97	1.36E-02	1.88
	64×64	7.15E-03	0.99	3.18E-02	0.96	8.36E-04	1.94	3.59E-03	1.92
10^{-2}	16×16	2.17E-02	-	1.07E-01	-	5.20E-03	-	3.21E-02	-
	32×32	1.09E-02	1.00	5.40E-02	0.99	2.20E-03	1.24	7.22E-03	2.15
	64×64	5.59E-03	0.96	2.60E-02	1.06	1.43E-03	0.62	4.13E-03	0.81
10^{-6}	16×16	2.17E-02	-	1.07E-01	-	4.68E-03	-	3.69E-02	-
	32×32	1.09E-02	1.00	5.42E-02	0.98	1.18E-03	1.98	9.90E-03	1.90
	64×64	5.48E-03	0.99	2.67E-02	1.02	2.97E-04	1.99	2.52E-03	1.97

Let $\sigma_s=1$, $\sigma_a=0$, then the source term S can be obtained via

$$S(t,x,y,v_x,v_y)=\partial_t f+\frac{1}{\varepsilon}\boldsymbol{v}\cdot\nabla_{\boldsymbol{x}} f+\frac{1}{\varepsilon^2}(f-\langle f\rangle). \tag{5.11}$$

As the source term S depends on time t and velocity $\boldsymbol{v}$, we derive an approximation model (5.12) instead of (5.9) via the same reformulation approach in Section 2, which is

$$\begin{aligned}\partial_t\rho+e^{-\sigma(t-t^n)/\varepsilon^2}\nabla_{\boldsymbol{x}}\cdot\langle\boldsymbol{v}g(t^n,\boldsymbol{x}^n,\boldsymbol{v})\rangle=&\nabla_{\boldsymbol{x}}\cdot\left(\frac{1}{\sigma}(1-e^{-\sigma(t-t^n)/\varepsilon^2})\nabla_{\boldsymbol{x}}\rho\right)-\sigma_a\rho+\langle S\rangle\\&-\varepsilon\nabla_{\boldsymbol{x}}\cdot\left(\frac{1}{\sigma}(1-e^{-\sigma(t-t^n)/\varepsilon^2})\langle\boldsymbol{v}S\rangle\right),\end{aligned} \tag{5.12a}$$

$$\partial_t f+\frac{1}{\varepsilon}\boldsymbol{v}\cdot\nabla_{\boldsymbol{x}} f=\frac{\sigma_s}{\varepsilon^2}(\rho-f)-\sigma_a f+S. \tag{5.12b}$$

For this test, we take $T=1.0$, $N_{\boldsymbol{v}}=590$, $\varepsilon=1,10^{-2},10^{-6}$ and $\Delta t=2.5h$. The results are shown in Table 5.5, which validate the desired convergence order of the proposed methods in both kinetic and diffusive regimes. Similarly, order reductions are observed in the intermediate regime due to the modeling approximation errors.

Secondly, we consider a Gaussian initial data centered at the origin with variance ζ^2 [51,27]

$$f(t=0,x,y,v_x,v_y)=\frac{1}{4\pi\zeta^2}\exp\left(-\frac{x^2+y^2}{4\zeta^2}\right), \tag{5.13}$$

and set $\sigma_a=0$, $S\equiv0$. We are interested in two challenging cases as follows:

Case 1: Spatially varying scattering coefficient σ_s in the intermediate regime. Let $\varepsilon=0.01$, $\sigma_a=S=0$, $\zeta^2=10^{-2}$ and σ_s varies in space as

$$\sigma_s(x,y)=\begin{cases}0.999c^4(c+\sqrt{2})^2(c-\sqrt{2})^2+0.001, & c=\sqrt{x^2+y^2}<1;\\ 1, & \text{otherwise.}\end{cases} \tag{5.14}$$

We take $N_x=N_y=128$, $N_v=590$. This is a challenging problem because the collision coefficient σ_s/ε varies in a large range $[0.1,100]$. For existing methods [22,23,45], they require a time step $\Delta t=0.1\min(\sigma_s)h^2+0.1\varepsilon h$, which is subject to a small time step in the intermediate regime. But as shown in Fig. 5.4, our methods are still stable with a ten times or a forty times larger time step. At the initial time layer, the first- and second-order schemes show no big difference. However, with such a large time step, the first-order SL-LDG-1 scheme has large deviation errors again. The second-order SL-LDG-2 scheme is better than the first-order scheme and is more accurate, even with large time steps.

Case 2: Line source problem. The line source problem describes an isotropic radiation impulse with total energy concentrated on the z-axis [53–56,51]. Hence, the initial data involves a Dirac delta function. For numerical simulations, we approximate the initial data by a steep Gaussian distribution (5.13) with $\zeta^2=3.2\times10^{-4}$. Besides, we set $\sigma_s=1$, $\sigma_a=0$, $S\equiv0$ and $\Omega_{\boldsymbol{x}}=[-0.6,0.6]^2$. We run the test with $\varepsilon=1$, $T=0.5$, $N_x=N_y=128$ and $N_v=5810$.

This example is in the kinetic regime and requires a large number of discrete ordinates to avoid a Ray effect [53,51]. This example shows the advantages of employing high order methods. As depicted in Fig. 5.5, the first-order method appears to converge not very well, and we can still observe some Ray effects, while the second-order method fits the physical solution much better under a large time step $\Delta t=2.5h$.

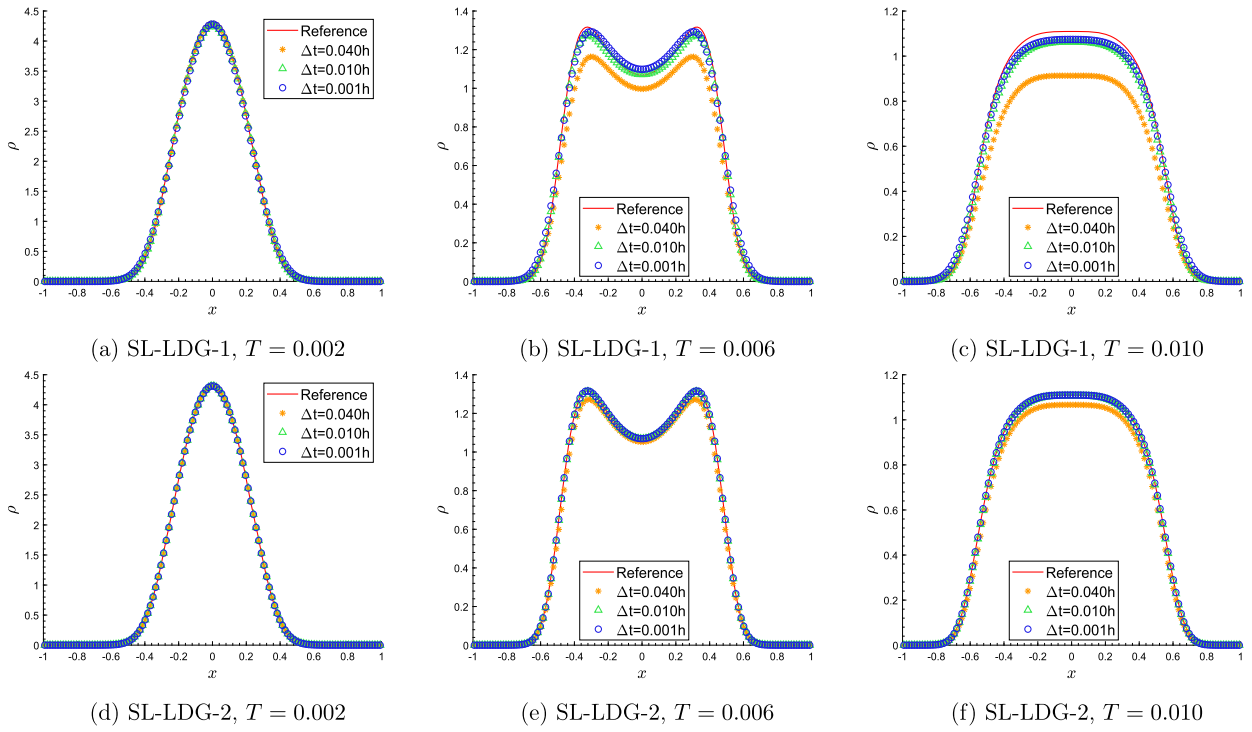

(a) SL-LDG-1, $T = 0.002$ (b) SL-LDG-1, $T = 0.006$ (c) SL-LDG-1, $T = 0.010$

(d) SL-LDG-2, $T = 0.002$ (e) SL-LDG-2, $T = 0.006$ (f) SL-LDG-2, $T = 0.010$

Fig. 5.4. Varying scattering problem for 2D transport problem (Section 5.2.1). Density ρ at $y = 0$ of the SL-LDG-p ($p = 1, 2$) solutions at $T = 0.002, 0.006, 0.010$ with $N_x = N_y = 128$, $N_{\boldsymbol{v}} = 590$ and different time steps Δt. The reference solutions are computed by the second-order finite difference method on staggered grids [52] with $h = 0.005$ and $\Delta t = 10^{-5}$.

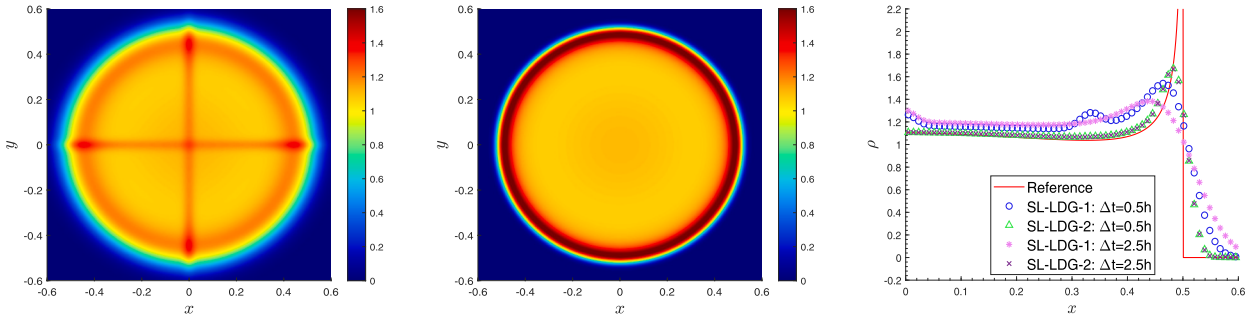

(a) SL-LDG-1, $\Delta t = 2.5h$ (b) SL-LDG-2, $\Delta t = 2.5h$ (c) Slices at $y = 0$

Fig. 5.5. Line source test for 2D transport problem (Section 5.2.1). Left and Middle: Density ρ of the SL-LDG-p ($p = 1, 2$) solutions at $T = 0.5$. Right: Slice at $y = 0$ with a reference solution from [57,58]. Parameters are $\varepsilon = 1$, $N_x = N_y = 128$, $N_{\boldsymbol{v}} = 5810$. $T = 0.5$.

5.2.2. 3D problem

Case 1: Accuracy test. Consider $\Omega_x = [-1, 1]^3$, $\sigma_s = 1$, $\sigma_a = 0$ and exact solution

$$\rho(t, x, y, z) = e^{-t} \sin(\pi x) \sin(\pi y) \sin(\pi z), \quad g = -(\boldsymbol{v} \cdot \nabla_{\boldsymbol{x}} \rho), \quad f = \rho + \varepsilon g. \tag{5.15}$$

The source term S is computed again by (5.12). We simulate with $N_{\boldsymbol{v}} = 170$, $\varepsilon = 1, 10^{-2}, 10^{-6}$, $T = 1.5$, $\Delta t = 2.5h$. In Table 5.6, the convergence orders for first-order and second-order schemes with different ε's are presented. The desired orders of accuracy with a large time step can be observed.

Case 2: Point source problem. Set $\varepsilon = 1$, $\Omega_{\boldsymbol{x}} = [-0.6, 0.6]^3$, $\sigma_s = 1$, $\sigma_a = 0$, $S \equiv 0$ and consider the following initial data:

$$f(t = 0, x, y, z, v_x, v_y, v_z) = \frac{1}{4\pi\zeta^2} \exp\left(-\frac{x^2 + y^2 + z^2}{4\zeta^2}\right), \quad \zeta^2 = 3.2 \times 10^{-4}. \tag{5.16}$$

Table 5.6
3D accuracy test (Section 5.2.2). Numerical errors and convergence orders of the SL-LDG-p ($p = 1, 2$) methods in L^1 and L^∞ norms. $T = 1.5$.

Parameter		$p=1$				$p=2$			
ϵ	$N_x \times N_y \times N_z$	$E^\rho_{N,1}$	$O^\rho_{N,1}$	$E^\rho_{N,\infty}$	$O^\rho_{N,\infty}$	$E^\rho_{N,1}$	$O^\rho_{N,1}$	$E^\rho_{N,\infty}$	$O^\rho_{N,\infty}$
1	$8\times8\times8$	1.93E-02	-	9.03E-01	-	3.24E-03	-	1.81E-01	-
	$16\times16\times16$	1.08E-02	0.83	5.98E-01	0.60	4.76E-04	2.77	3.00E-02	2.59
	$32\times32\times32$	5.55E-03	0.97	3.10E-01	0.95	1.09E-04	2.13	5.38E-03	2.48
10^{-2}	$8\times8\times8$	4.08E-03	-	1.87E-01	-	1.27E-03	-	9.70E-02	-
	$16\times16\times16$	1.99E-03	1.03	8.93E-02	1.06	3.23E-04	1.98	2.71E-02	1.84
	$32\times32\times32$	9.90E-04	1.01	4.44E-02	1.01	8.64E-05	1.90	7.41E-03	1.87
10^{-6}	$8\times8\times8$	4.08E-03	-	1.86E-01	-	1.28E-03	-	9.75E-02	-
	$16\times16\times16$	1.99E-03	1.03	8.91E-02	1.06	3.28E-04	1.96	2.75E-02	1.82
	$32\times32\times32$	9.90E-04	1.01	4.44E-02	1.00	8.32E-05	1.98	7.16E-03	1.94

Table 5.7
3D Point source problem (Section 5.2.2). Parallel efficiency of the SL-LDG-2 method. Parameters are $N_x = N_y = N_z = 50$, $N_{\boldsymbol{v}} = 1202$, $T = 0.5$ and $\Delta t = 0.025$. P is the number of threads; RT is the running time; S is the speedup ratio; E is the parallel efficiency. The time unit is second.

P	RT_{total}	S_{total}	E_{total}	RT_ρ	S_ρ	E_ρ	RT_f	S_f	E_f
1	13552.66	-	-	8364.99	-	-	4163.34	-	-
2	6835.17	1.98	99.14%	3947.65	2.12	105.95%	2297.08	1.81	90.62%
4	3512.93	3.86	96.45%	1931.29	4.33	108.28%	1247.16	3.34	83.46%
8	1641.28	8.26	103.22%	764.02	10.95	136.86%	647.89	6.43	80.32%
16	1047.95	12.93	80.83%	466.11	17.95	112.17%	355.25	11.72	73.25%

Here we compare the numerical behavior of the SL-LDG-2 method with that of the StaRMAP method [52]. The StaRMAP method solves the spherical harmonics moment (P_N) systems using a second-order staggered grid finite difference method [59]. In the simulation, we take the StaRMAP method by setting $N = 600$ in P_N, while $N = N_{\boldsymbol{v}} = 1202$ in S_N for our SL-LDG-2 method with comparable degrees of freedom. We take the mesh size $h = 0.024$ and time step $\Delta t = 1/128$. As depicted in Fig. 5.6, the StaRMAP solution exhibits notable numerical oscillations due to the wave effect of the P_N method. Our method is almost oscillation-free, but it exhibits a little ray effect due to the S_N method.

Secondly, we evaluate the parallel efficiency of the proposed methods with an OpenMP API. We refer to an R-step for solving the macroscopic equation and an F-step for solving the microscopic equation. In the R-step, the transport term involves a numerical integration in velocity, which can be computed in a parallel way. In the F-step, the distribution function with different velocities can be updated simultaneously since the density is known. As illustrated in Table 5.7, the speedup trend for the F-step parallelization is nearly linear. Surprisingly, the R-step parallelization enjoys superlinear speedup. This remarkable performance can be attributed to the efficient cache exploitation on a shared memory architecture [60,61]. As a result, we have significantly reduced the total runtime from 13552.66 seconds (225.87 minutes) to 1047.95 seconds (17.47 minutes) via the multi-threading technique (single thread to 16 threads). In other words, the computational speed increased by more than 10 times.

Remark 5.1. Here we briefly discuss the memory usage of the proposed methods. Taking a uniform rectangular mesh as an example, we denote d as the number of spatial dimensions, N_x as the number of cells along each spatial dimension and N_{dof} as the number of degrees of freedom (DoFs) per element in a DG method. In particular, $N_{dof} = \frac{(k+d)!}{d!}$ for a $\mathcal{P}^k$ polynomial space. We recall $N_{\boldsymbol{v}}$ is the number of discrete velocities. Firstly, the two main unknowns f and ρ consume the most storage in the size of $O(N_{\boldsymbol{v}} N_x^d N_{\text{dof}})$. Secondly, diffusion operators $l_K(\cdot,\cdot)$ and $d_K(\cdot,\cdot)$ in (3.10) need $O(N_x^d N_{\text{dof}}^2)$ for sparse matrices storage. Thirdly, the action of operators $b_K(\cdot,\cdot)$ in (3.10) and $a_K(\cdot,\cdot)$ in (3.21) on the DoFs of f and ρ is equivalent to matrix-vector products. The underlying matrices involve integrals of type (c) and (d) in Remark 3.1, which depend on the time step size. If a uniform time step is used, we may store these integrals once so as to significantly reduce computational cost. For a uniform rectangular mesh, integral evaluation only needs to be done within a hypercube $[0,1]^d$ for each discrete velocity. With a fixed velocity, through the clipping operation, there are at most $N_e = 2^d$ sub-elements and $N_f = d2^d$ sub-faces generated. The operator $a_K(\cdot,\cdot)$ stores 1 matrix of volume integrals at each sub-element. The operator $b_K(\cdot,\cdot)$ stores d matrices of volume integrals at each sub-element and 1 matrix of flux integrals at each sub-face. Each matrix is of shape $N_{dof} \times N_{dof}$. As a result, the total storage for operators $b_K(\cdot,\cdot)$ and $a_K(\cdot,\cdot)$ is no more than $((d+1)N_e + N_f)N_{\boldsymbol{v}} N_{dof}^2 = (2d+1)2^d N_{\boldsymbol{v}} N_{dof}^2$. In summary, the most storage is for the two main unknowns f and ρ, which is in the size of $O(N_{\boldsymbol{v}} N_x^d N_{\text{dof}})$. Taking the 3D point source problem as an example, with $N_x = N_y = N_z = 50$, $N_{\boldsymbol{v}} = 1202$ and $d = 3$, it costs about 17.91 GB for the storage of two main unknowns f and ρ in a double precision floating point. The storage would increase rapidly with mesh refinement. How to reduce the memory usage in our method will be studied in our future work.

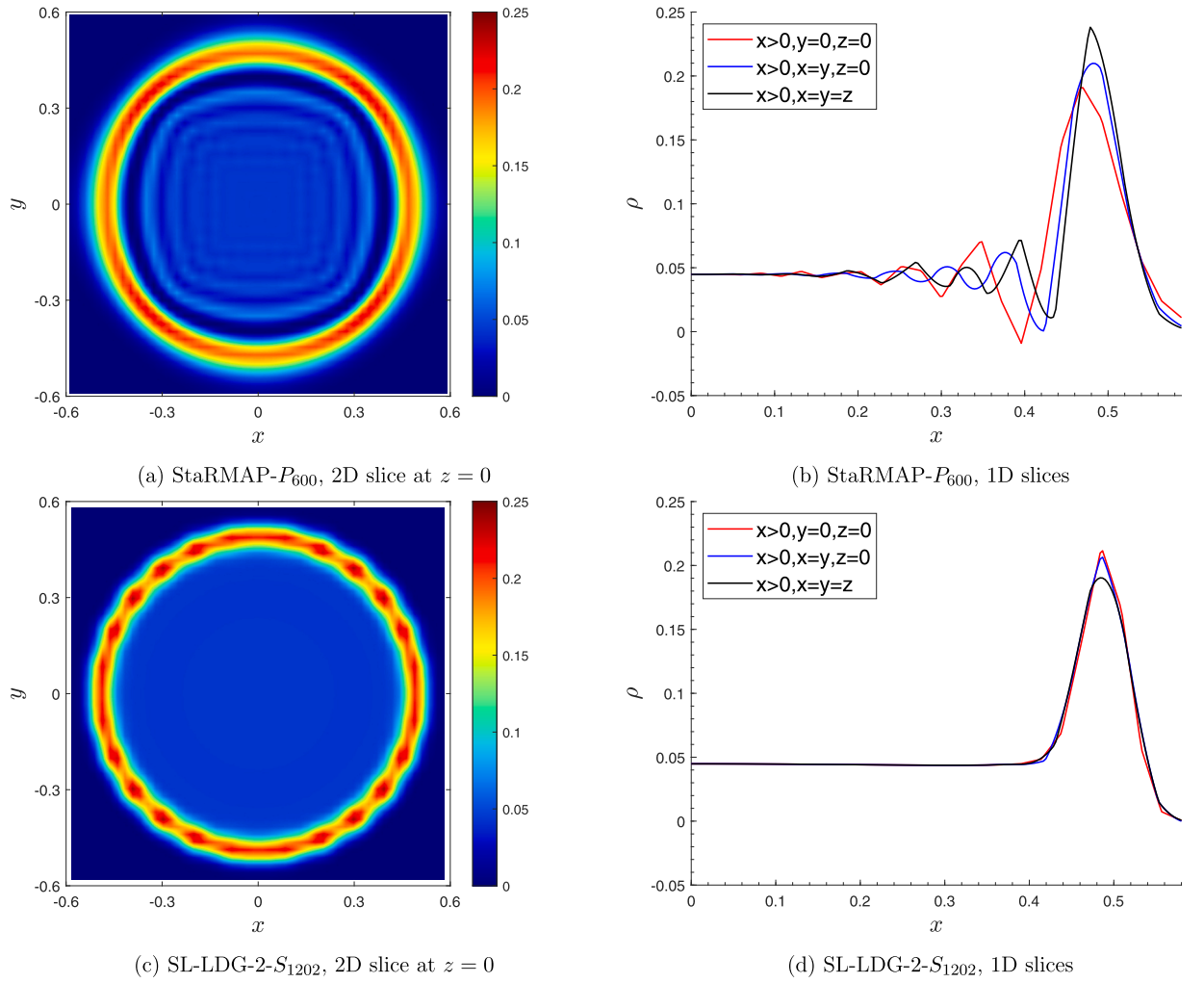

(a) StaRMAP-P_{600}, 2D slice at $z = 0$

(b) StaRMAP-P_{600}, 1D slices

(c) SL-LDG-2-S_{1202}, 2D slice at $z = 0$

(d) SL-LDG-2-S_{1202}, 1D slices

Fig. 5.6. 3D Point source problem (Section 5.2.2). Comparison of the StaRMAP and SL-LDG-2 solutions at $T = 0.5$. (a) (b): Density plots of the StaRMAP solution for a P_{600} system. (c) (d): Density plots of the SL-LDG-2 solution for a S_{1202} system ($N_v = 1202$). Both tests are run with $N_x = N_y = N_z = 50$ and $\Delta t = T/64$.

Case 3: Varying scattering problem in the intermediate regime. Finally we consider a 3D extension of Case 1 in Section 5.2.1. With such an example, we can clearly see the superiority of our methods for solving such problems in the intermediate regime. Set $\Omega_{\boldsymbol{x}} = [-1, 1]^3$, $\sigma_a = S = 0$, $\varepsilon = 0.01$ and

$$\sigma_s(x, y, z) = \begin{cases} 0.999c^4(c + \sqrt{2})^2(c - \sqrt{2})^2 + 0.001, & c = \sqrt{x^2 + y^2 + z^2} < 1; \\ 1, & \text{otherwise.} \end{cases} \tag{5.17}$$

The initial condition is still (5.16) but with $\zeta^2 = 10^{-2}$. We also compare the proposed SL-LDG-2 method with the StaRMAP method. The StaRMAP method is only available for $\varepsilon = 1$. To make a comparison, we scaled the termination time and scattering coefficient by taking $T^{StaRMAP} = T/\varepsilon$ and $\sigma_s^{StaRMAP} = \sigma_s/\varepsilon^2$, where T, σ_s are used for the SL-LDG-2 method. Besides, we solve a P_{13} system for the StaRMAP method and a S_{194} system for the SL-LDG-2 method, with comparable degrees of freedom in the velocity space. The numerical results are presented in Fig. 5.7. Here we fix the final time T but take different time steps to arrive at the final time, corresponding to different time step sizes. The two methods perform similarly with small time steps. However, with a larger time step, the StaRMAP method would blow up after some time, while the SL-LDG-2 method remains stable and matches the reference solution well.

6. Conclusions and outlook

In this paper, we have developed a class of uniformly unconditionally stable AP SL DG methods for solving kinetic transport equations under a diffusive scaling. We design both first-order and second-order SL DG methods for an approximation model, leveraging the strength of SL techniques in a weak DG formulation to enhance computational efficiency. Furthermore, within the

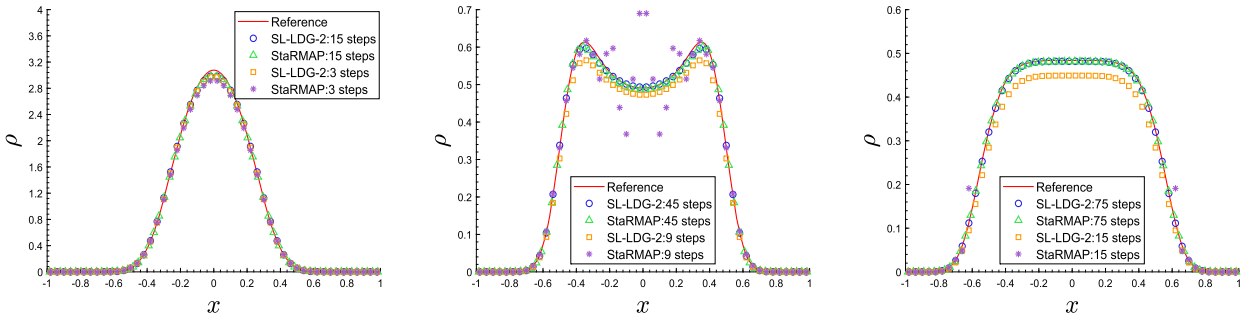

(a) $T = 0.002$ (b) $T = 0.006$ (c) $T = 0.010$

Fig. 5.7. Varying scattering problem for 3D transport problem (Section 5.2.2). Comparison of the SL-LDG-2 method and StaRMAP method under different time steps. Density profile ρ at $y = z = 0$ is plotted at $T = 0.002, 0.006, 0.010$. Parameters are $\varepsilon = 0.01, N_x = N_y = N_z = 50$. The StaRMAP solutions are for P_{13} system while SL-LDG-2 solutions are for S_{194} system ($N_v = 194$). The reference solutions are computed by a first-order finite difference method on staggered grids with $N_x = N_y = N_z = 150$ and $\Delta t = 0.1\varepsilon h + 0.1h^2$.

DG framework, it is possible to utilize an oscillation-free damping limiter in tandem with an implicit time discretization, surpassing the performance of conventional slope limiters. Numerical experiments spanning from 1D to 3D problems have provided empirical validation of the expected orders of accuracy, robustness, and high parallel efficiency inherent in our methods. The effectiveness and efficiency of our proposed approaches are particularly pronounced when addressing high-dimensional multiscale problems.

In the future, it would be intriguing to explore more general collision operators, such as those associated with frequency-dependent kinetic problems. Additionally, we plan to investigate uniformly unconditional stability through energy stability analyses.

CRediT authorship contribution statement

Yi Cai: Writing – review & editing, Writing – original draft, Visualization, Methodology, Formal analysis, Conceptualization. **Guoliang Zhang:** Writing – original draft, Methodology, Formal analysis, Conceptualization. **Hongqiang Zhu:** Writing – review & editing, Methodology, Formal analysis, Conceptualization. **Tao Xiong:** Writing – review & editing, Writing – original draft, Supervision, Methodology, Funding acquisition, Conceptualization.

Declaration of competing interest

The authors declare that they have no known competing financial interests or personal relationships that could have appeared to influence the work reported in this paper.

Data availability

Data will be made available on request.

Acknowledgements

We acknowledge the computing resource and technical support provided by Tan Kah Kee Supercomputing Center (IKKEM) in Xiamen University.

Appendix A. Proof of Lemma 2.1

Proof. Let $E(s) := \int_0^s e^{-\alpha(s-\tau)}(\eta(\tau) - \eta(s))\,\mathrm{d}\tau$, and by using the Taylor series expansion we have

$$\begin{aligned} E(s) &= \int_0^s e^{-\alpha(s-\tau)} \left[\sum_{i=1}^{\infty} \frac{(-1)^i (s-\tau)^i}{i!} \eta^{(i)}(s) \mathrm{d}\tau \right] \\ &= \sum_{i=1}^{\infty} \frac{(-1)^i}{i!} \eta^{(i)}(s) \int_0^s e^{-\alpha(s-\tau)} (s-\tau)^i \mathrm{d}\tau \\ &= \sum_{i=1}^{\infty} \frac{(-1)^i}{\beta^{i+1} i!} \beta^{i+1} \eta^{(i)}(s) \int_0^s e^{-\alpha(s-\tau)} (s-\tau)^i \mathrm{d}\tau. \end{aligned} \tag{A.1}$$

The parameter β^{i+1} is added to match the scale of $\eta^{(i)}(s)$. As we can see, we will take $\beta=\varepsilon$ in (B.1) in the proof of Theorem 2.2. We denote $A_i=\int_0^s e^{-\alpha(s-\tau)}(s-\tau)^i \mathrm{d}\tau$ and $B_i=s^i e^{-\alpha s}$, and by mathematical induction we obtain

$$B_0=e^{-\alpha s},\quad A_0=\alpha^{-1}(1-B_0),\quad A_i=\alpha^{-1}\left(iA_{i-1}-B_i\right),\quad i\geq 1. \tag{A.2}$$

This relation also yields

$$A_i=\alpha^{-1}\left(\alpha^{-i}(i!)-\sum_{j=0}^{i}\frac{i!}{(i-j)!}\alpha^{-j}B_{i-j}\right)=\alpha^{-(i+1)}(i!)\left(1-\sum_{j=0}^{i}\frac{\alpha^j}{j!}B_j\right). \tag{A.3}$$

Then, we have

$$E(s)=\sum_{i=1}^{\infty}\beta^{-(i+1)}C_iD_i,\quad C_i=(-1)^i\alpha^{-(i+1)}\beta^{i+1}\eta^{(i)}(s),\quad D_i=1-\sum_{j=0}^{i}\frac{\alpha^j}{j!}B_j, \tag{A.4}$$

and by the assumption $\left|\beta^{i+1}\eta^{(i)}(s)\right|\leq M$ for all $i\geq 1$,

$$\left|C_i\right|\leq\alpha^{-(i+1)}M,\quad \left|D_i\right|=e^{-\alpha s}\left(e^{\alpha s}-\sum_{j=0}^{i}\frac{(\alpha s)^j}{j!}\right)=e^{-\alpha s}\sum_{j=i+1}^{\infty}\frac{(\alpha s)^j}{j!},\quad 0<D_i<1. \tag{A.5}$$

With these, we arrive at

$$\begin{aligned}|E(s)|&\leq\sum_{i=1}^{\infty}\left|C_i\right|\left|D_i\right|\leq Me^{-\alpha s}\sum_{i=1}^{\infty}\sum_{j=i+1}^{\infty}(\alpha\beta)^{-(i+1)}\frac{(\alpha s)^j}{j!}\\&=Me^{-\alpha s}\sum_{i=2}^{\infty}\sum_{j=i}^{\infty}\frac{(\alpha\beta)^{-i}(\alpha s)^j}{j!}\\&=Me^{-\alpha s}\sum_{j=2}^{\infty}\sum_{i=2}^{j}\frac{(\alpha\beta)^{-i}(\alpha s)^j}{j!}=:MU(\alpha,\beta,s).\end{aligned} \tag{A.6}$$

Let $u=(\alpha\beta)^{-1}$ and $v=\alpha s$, we rewrite the upper bound U as follows:

$$U=e^{-\alpha s}\sum_{j=2}^{\infty}\sum_{i=2}^{j}\frac{(\alpha\beta)^{-i}(\alpha s)^j}{j!}=e^{-v}\sum_{j=2}^{\infty}\sum_{i=2}^{j}\frac{u^iv^j}{j!}=e^{-v}\sum_{j=2}^{\infty}\frac{w_jv^j}{j!} \tag{A.7}$$

where

$$w_j=\begin{cases}\frac{u^2(1-u^{j-1})}{1-u}, & u\neq 1;\\ j-1, & u=1.\end{cases} \tag{A.8}$$

When $u=1$, we have

$$\begin{aligned}U&=e^{-v}\sum_{j=2}^{\infty}\frac{(j-1)v^j}{j!}=v^2e^{-v}\sum_{j=2}^{\infty}\frac{\mathrm{d}}{\mathrm{d}v}\left(\frac{v^{j-1}}{j!}\right)=v^2e^{-v}\frac{\mathrm{d}}{\mathrm{d}v}\left(v^{-1}\sum_{j=2}^{\infty}\frac{v^j}{j!}\right)\\&=v^2e^{-v}\frac{\mathrm{d}}{\mathrm{d}v}\left(v^{-1}(e^v-1-v)\right)=e^{-v}-1+v=e^{-\alpha s}-1+\alpha s.\end{aligned} \tag{A.9}$$

When $u\neq 1$, we get

$$\begin{aligned}U&=\frac{u^2e^{-v}}{1-u}\sum_{j=2}^{\infty}\frac{(1-u^{j-1})v^j}{j!}=\frac{u^2e^{-v}}{1-u}\left[\sum_{j=2}^{\infty}\frac{v^j}{j!}-u^{-1}\sum_{j=2}^{\infty}\frac{(uv)^j}{j!}\right]\\&=\frac{u^2e^{-v}}{1-u}\left[(e^v-1-v)-u^{-1}(e^{uv}-1-uv)\right]=\frac{u^2e^{-v}}{1-u}\left[e^v-1-u^{-1}e^{uv}+u^{-1}\right]\\&=\frac{u^2(1-e^{-v})}{1-u}+\frac{ue^{-v}(1-e^{uv})}{1-u}=\frac{(\alpha\beta)^{-2}(1-e^{-\alpha s})}{1-(\alpha\beta)^{-1}}+\frac{(\alpha\beta)^{-1}(e^{-\alpha s}-e^{-(\alpha-\beta^{-1})s})}{1-(\alpha\beta)^{-1}}.\end{aligned} \tag{A.10}$$

□

Appendix B. Proof of Theorem 2.2

Proof. Let $\tau=t-t_0, s=t_1-t_0=\Delta t, \eta(\tau)=\frac{\mathrm{d}\rho}{\mathrm{d}\tau}(\tau), \alpha=\varepsilon^{-2}, \beta=\varepsilon$. The assumption $\left|\beta^{i+1}\eta^{(i)}(s)\right|\leq M$ now becomes:

$$\left|\beta^{k+1}\eta^{(k)}(s)\right|=\left|(\varepsilon\partial_t+\boldsymbol{v}\cdot\nabla_{\boldsymbol{x}})^{k+1}\rho(s)\right|\leq M,\quad\forall k\geq 1. \tag{B.1}$$

By Lemma 2.1, we have

$$\begin{aligned}\|\boldsymbol{F}-\boldsymbol{G}\|_\infty &\le \left|\left\langle \frac{\|\boldsymbol{v}\|_\infty}{\varepsilon}\int_{t_0}^{t_1} e^{-(t_1-t)/\varepsilon^2}\left(\frac{\mathrm{d}\rho}{\mathrm{d}t}(t)-\frac{\mathrm{d}\rho}{\mathrm{d}t}(t_1)\right)\mathrm{d}t\right\rangle\right| \\ &= \left|\left\langle \frac{\|\boldsymbol{v}\|_\infty}{\varepsilon}\int_0^{s} e^{-(s-\tau)/\varepsilon^2}(\eta(\tau)-\eta(s))\mathrm{d}\tau\right\rangle\right| \\ &\le \left\langle \frac{\|\boldsymbol{v}\|_\infty}{\varepsilon}\left|\int_0^{s} e^{-(s-\tau)/\varepsilon^2}(\eta(\tau)-\eta(s))\mathrm{d}\tau\right|\right\rangle \\ &\le \frac{\langle\|\boldsymbol{v}\|_\infty\rangle}{\varepsilon}\boldsymbol{M}\boldsymbol{U}(\varepsilon,\Delta t)=\boldsymbol{C}\boldsymbol{W}(\varepsilon,\Delta t)\end{aligned} \tag{B.2}$$

where $\|\boldsymbol{x}\|_\infty=\max_i|x_i|$, $C=\langle\|\boldsymbol{v}\|_\infty\rangle M>0$ is a constant independent of ε and Δt; $W(\varepsilon,\Delta t)$ is given as follows:

$$W(\varepsilon,\Delta t)=\frac{1}{\varepsilon}U(\varepsilon,\Delta t)=\begin{cases} e^{-\Delta t}-1+\Delta t, & \varepsilon=1;\\ \frac{\varepsilon(1-e^{-\Delta t/\varepsilon^2})}{1-\varepsilon}-\frac{e^{-(1-\varepsilon)\Delta t/\varepsilon^2}-e^{-\Delta t/\varepsilon^2}}{1-\varepsilon}, & \varepsilon\neq 1.\end{cases} \tag{B.3}$$

(1) For $\varepsilon=1$, from a Taylor series expansion of $e^{-\Delta t}$, (B.3) implies that $\|\boldsymbol{F}-\boldsymbol{G}\|_\infty=O(\Delta t^2)$ as $\Delta t\to 0$. (2) For $0<\varepsilon<1$, on the one hand, we have $W(\varepsilon,\Delta t)<\frac{\varepsilon}{1-\varepsilon}$ as $e^{-(1-\varepsilon)\Delta t/\varepsilon^2}>e^{-\Delta t/\varepsilon^2}$; On the other hand, we also have $W(\varepsilon,\Delta t)=O(\varepsilon^{-3}\Delta t^2)$ if $\Delta t<\varepsilon^2$. In fact, from $e^x=\sum_{n=0}^{\infty}\frac{1}{n!}x^n$ for all $x\in\mathbb{R}$, we get

$$\begin{aligned}W(\varepsilon,\Delta t)&=\frac{1}{1-\varepsilon}\left[\varepsilon\left(1-\sum_{n=0}^{\infty}\frac{1}{n!}(-\frac{\Delta t}{\varepsilon^2})^n\right)-\sum_{n=0}^{\infty}\frac{1}{n!}((1-\varepsilon)^n-1)(-\frac{\Delta t}{\varepsilon^2})^n\right]\\ &=\frac{1}{1-\varepsilon}\left[-\varepsilon\left(\sum_{n=1}^{\infty}\frac{1}{n!}(-\frac{\Delta t}{\varepsilon^2})^n\right)+\sum_{n=1}^{\infty}\frac{1}{n!}(1-(1-\varepsilon)^n)(-\frac{\Delta t}{\varepsilon^2})^n\right]\\ &=\sum_{n=2}^{\infty}\frac{(-1)^n}{n!}(1-(1-\varepsilon)^{n-1})(\frac{\Delta t}{\varepsilon^2})^n\\ &=\frac{1}{2}\varepsilon^{-3}\Delta t^2-\sum_{k=1}^{\infty}(a_{2k+1}-a_{2k+2}),\end{aligned}$$

where

$$a_{2k+1}=\frac{1-(1-\varepsilon)^{2k}}{(2k+1)!}\left(\frac{\Delta t}{\varepsilon^2}\right)^{2k+1}.$$

We will show that $a_{2k+1}>a_{2k+2}$ for all $k\ge 1$. Let us define

$$u(k)=(2k+2)\frac{1-(1-\varepsilon)^{2k}}{1-(1-\varepsilon)^{2k+1}}. \tag{B.4}$$

We can verify that $u'(k)>0$ for all $k\ge 1$ if $0<\varepsilon<1$, so $u(k)$ is monotonically increasing. Then $u(k)\ge u(1)=\frac{4(1-(1-\varepsilon)^2)}{1-(1-\varepsilon)^3}>1>\Delta t/\varepsilon^2$. This implies that $a_{2k+1}>a_{2k+2}$ for any $k\ge 1$. Hence $W(\varepsilon,\Delta t)<\frac{1}{2}\varepsilon^{-3}\Delta t^2$ if $\Delta t<\varepsilon^2$.

In summary, we arrive at an upper bound for $W(\varepsilon,\Delta t)$,

$$W^*(\varepsilon,\Delta t)=\begin{cases}\frac{\Delta t^2}{2\varepsilon^3}, & \text{if } \Delta t\le\varepsilon^2;\\ \frac{\varepsilon}{1-\varepsilon}, & \text{if } \Delta t>\varepsilon^2.\end{cases} \tag{B.5}$$

As a consequence, we get that for $\varepsilon\in(0,1)$, $\|\boldsymbol{F}-\boldsymbol{G}\|_\infty=O(\varepsilon^{-3}\Delta t^2)$ if $\Delta t\le\varepsilon^2$ and $\|\boldsymbol{F}-\boldsymbol{G}\|_\infty=O(\frac{\varepsilon}{1-\varepsilon})$ otherwise. Furthermore, from the Fig. B.1, it shows that $W^*(\varepsilon,\Delta t)$ is a very sharp upper bound of $W(\varepsilon,\Delta t)$. □

Appendix C. Proof of Theorem 4.2

Proof. First, we consider the SL1-LDGq method (3.32) and examine how each term contributes to the amplification matrix. For the diffusion term, with (4.1), we have

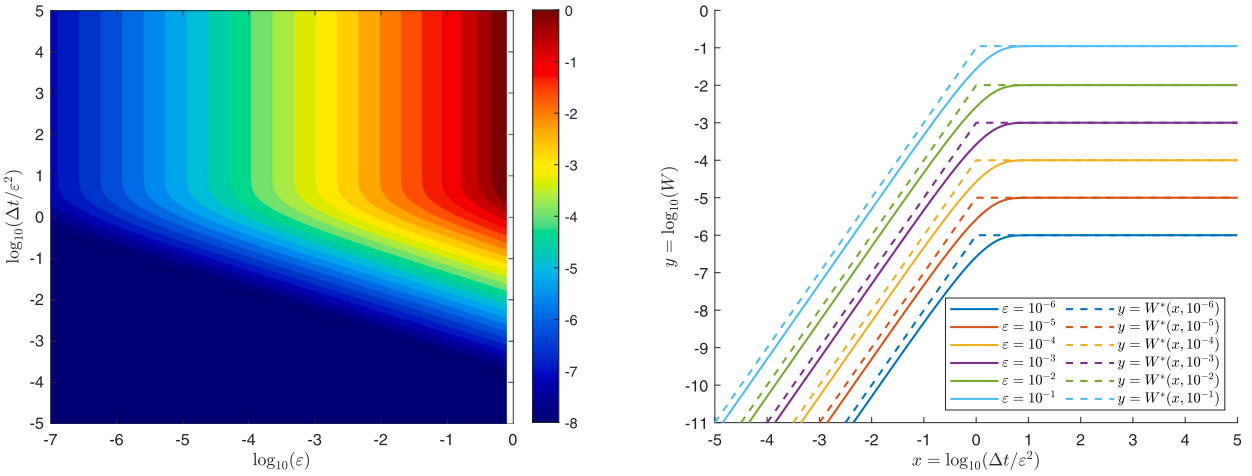

Fig. B.1. Left: 2D contour of $W(\varepsilon, \Delta t)$; Right: comparison of $W(\varepsilon, \Delta t)$ and $W^*(\varepsilon, \Delta t)$. A colored solid line represents the slice of W at a given ε, while a dashed line with the same color represents the slice of upper bound W^* at the same ε.

$$r_{I_i}(\tilde{\rho}_h^{n+1}, \phi_i^j) = \sum_{l=0}^{q-1} \tilde{\rho}_{i,l}^{n+1} \phi_i^l(x^-_{i+\frac{1}{2}}) \phi_i^j(x^-_{i+\frac{1}{2}}) - \sum_{l=0}^{q-1} \tilde{\rho}_{i-1,l}^{n+1} \phi_{i-1}^l(x^-_{i-\frac{1}{2}}) \phi_i^j(x^+_{i-\frac{1}{2}}) - \sum_{l=0}^{q-1} \tilde{\rho}_{i,l}^{n+1} \int_{I_i} \phi_i^l(x) \partial_x \phi_i^j(x) \mathrm{d}x. \tag{C.1}$$

Substituting the ansatz $\tilde{\rho}_{i,l}^n = \hat{\tilde{\rho}}_l^n \exp(\mathcal{I}\kappa x_i)$ into (C.1) and use $\phi_i^l(x) = \phi^l(\xi_i)$ with $\xi = \frac{x - x_i}{h}$, we obtain

$$r_{I_i}(\tilde{\rho}_h^{n+1}, \phi_i^j) = \exp(\mathcal{I}\kappa x_i) \sum_{l=0}^{q-1} R_{j,l}(\omega) \hat{\tilde{\rho}}_l^{n+1}, \tag{C.2}$$

where

$$R_{j,l}(\omega) = \phi^l(\frac{1}{2}) \phi^j(\frac{1}{2}) - \exp(-\mathcal{I}\omega) \phi^l(\frac{1}{2}) \phi^j(-\frac{1}{2}) - \int_{-1/2}^{1/2} \phi^l(\xi) \partial_\xi \phi^j(\xi) \mathrm{d}\xi.$$

We denote $\boldsymbol{R}(\omega) = (R_{j,l}(\omega)) \in \mathbb{R}^{q \times q}$. Similarly, there exists $\boldsymbol{L}(\omega) = (L_{j,l}(\omega)) \in \mathbb{R}^{q \times q}$, such that

$$\left(\mathcal{D}_h^q q_h^{n+1}, \phi_i^j \right)_{I_i} = \exp(\mathcal{I}\kappa x_i) \sum_{l=0}^{k-1} L_{j,l}(\omega) \hat{q}_l^{n+1}. \tag{C.3}$$

For the convection term, we denote $x^* = x - v\Delta t/\epsilon$ and define an operator $\mathcal{D}_{h,v}^g : U_h^{q-1} \to U_h^{q-1}$ for a given positive velocity $v > 0$ (the case of negative velocity is similar), such that

$$(\mathcal{D}_{h,v}^g g_h^n(\cdot, v), \phi_i^j)_{I_i} = \sum_{l=0}^{q-1} g_{i+m_{S-1},l}^n \phi_{i+m_{S-1}}^l(x^{*,-}_{i+\frac{1}{2}}) \phi_i^j(x^-_{i+\frac{1}{2}}) - \sum_{l=0}^{q-1} g_{i+m_0,l}^n \phi_{i+m_0}^j(x^{*,-}_{i-\frac{1}{2}}) \phi_i^j(x^+_{i-\frac{1}{2}}) - \sum_{s=0}^{S-1} \sum_{l=0}^{q-1} g_{i+m_s,l}^n \int_{J_{i,s}} \phi_{i+m_s}^l(x^*) \partial_x \phi_i^j(x) \mathrm{d}x. \tag{C.4}$$

Here we assume that an element I_i at t^{n+1} is splitted into S segments, denoted by $J_{i,s}$ for $s = 0, \ldots, S-1$. Each $J_{i,s}$ is tracked as an upstream segment $J_{i,s}^*$ contained in an element I_{i+m_s} at t^n, resulting in an upstream element I_i^*. Thanks to the constant velocity v, I_i is not out of shape when tracking along characteristic lines, so that $S \le 2$ in the one-dimensional case. We claim that there exists $\boldsymbol{H}(\omega, \frac{\Delta t}{\varepsilon h}; v) \in \mathbb{R}^{q \times q}$, such that

$$(\mathcal{D}_{h,v}^g g_h^n(\cdot, v), \phi_i^j)_{I_i} = \exp(\mathcal{I}\kappa x_i) \sum_{l=0}^{q-1} H_{j,l}(\omega, \frac{\Delta t}{\varepsilon h}; v) \hat{g}_l^n. \tag{C.5}$$

(1) When $S=1$, $\frac{v\Delta t}{\varepsilon h}$ is an integer, then (C.4) can be written as (C.5) with

$$\begin{aligned} H_{j,l}(\omega,\frac{\Delta t}{\varepsilon h};v) &= \exp(\mathcal{I}m\omega)\phi^l(\frac{1}{2})\phi^j(\frac{1}{2}) - \exp(\mathcal{I}(m-1)\omega)\phi^l(\frac{1}{2})\phi^j(-\frac{1}{2}) \\ &\quad - \exp(\mathcal{I}m\omega)\int_{-\frac{1}{2}}^{\frac{1}{2}}\phi^l(\xi)\phi^j(\xi)\mathrm{d}\xi, \quad \text{where } m=-\frac{v\Delta t}{\varepsilon h}. \end{aligned} \tag{C.6}$$

(2) When $S=2$, we set $J_{i,0}=[x_{i-\frac{1}{2}},\hat{x}]$ and $J_{i,1}=[\hat{x},x_{i+\frac{1}{2}}]$. With a given velocity v, we first find the reference coordinate $\hat{\xi}=\frac{\hat{x}-x_i}{h}$ of $\hat{x}$ with respect to I_i as follows. Let $x^*_{i-\frac{1}{2}}<\hat{x}^*=x_{i+m+\frac{1}{2}}<x^*_{i+\frac{1}{2}}$ and then $m=-\left\lfloor\frac{v\Delta t}{\varepsilon h}\right\rfloor-1$,

$$\hat{\xi}=\frac{\hat{x}-x_i}{h}=\frac{\hat{x}^*-x_i^*}{h}=-\frac{1}{2}+\left(\frac{v\Delta t}{\varepsilon h}-\left\lfloor\frac{v\Delta t}{\varepsilon h}\right\rfloor\right)\in[-\frac{1}{2},\frac{1}{2}]. \tag{C.7}$$

Therefore, in the reference coordinate, an element I_i at t^{n+1} is splitted into $\hat{J}_{i,0}=[-\frac{1}{2},\hat{\xi}]$ and $\hat{J}_{i,1}=[\hat{\xi},\frac{1}{2}]$. In addition, an element I_i^* at t^n is splitted into $J^*_{i,0}=[x^*_{i-\frac{1}{2}},\hat{x}^*]$ and $J^*_{i,1}=[\hat{x}^*,x^*_{i+\frac{1}{2}}]$, where

$$x_{i+m_0-\frac{1}{2}}<x^*_{i-\frac{1}{2}}<x_{i+m_0+\frac{1}{2}}, \quad x_{i+m_1-\frac{1}{2}}<x^*_{i+\frac{1}{2}}<x_{i+m_1+\frac{1}{2}}. \tag{C.8}$$

Let $\lfloor x\rfloor$ denote the floor of x, we get

$$m_0=-\left\lfloor\frac{v\Delta t}{\varepsilon h}\right\rfloor-1, \quad m_1=-\left\lfloor\frac{v\Delta t}{\varepsilon h}\right\rfloor. \tag{C.9}$$

We next compute the reference coordinates of $J^*_{i,s}$ with respect to I_{i+m_s}. Firstly, let $x\in J_{i,0}$, $x^*\in J^*_{i,0}$ and $\xi=\frac{x-x_i}{h}\in\hat{J}_{i,0}$. With (C.7), we get

$$\frac{x^*-x_{i+m_0}}{h}=\frac{x-x_i}{h}-\left(\frac{v\Delta t}{\varepsilon h}-\left\lfloor\frac{v\Delta t}{\varepsilon h}\right\rfloor-1\right)=\xi-\hat{\xi}+\frac{1}{2}\in[-\hat{\xi},\frac{1}{2}]=:\hat{J}^*_{i,0}. \tag{C.10}$$

This means that the reference coordinate of a point $x^*\in J^*_{i,0}$ with respect to I_{i+m_s} locates within $\hat{J}^*_{i,0}$. Similarly, we can derive that

$$\frac{x^*-x_{i+m_1}}{h}=\frac{x-x_i}{h}-\left(\frac{v\Delta t}{\varepsilon h}-\left\lfloor\frac{v\Delta t}{\varepsilon h}\right\rfloor\right)=\xi-\hat{\xi}-\frac{1}{2}\in[-\frac{1}{2},-\hat{\xi}]=:\hat{J}^*_{i,1}. \tag{C.11}$$

At this end, we can rewrite (C.4) in the form of (C.5) with

$$\begin{aligned} H_{j,l}(\omega,\frac{\Delta t}{\varepsilon h};v) &= \exp(\mathcal{I}m_1\omega)\phi^l(-\hat{\xi})\phi^j(\frac{1}{2}) - \exp(\mathcal{I}m_0\omega)\phi^l(-\hat{\xi})\phi^j(-\frac{1}{2}) \\ &\quad - \exp(\mathcal{I}m_0\omega)\int_{-\frac{1}{2}}^{\hat{\xi}}\phi^l(\xi-\hat{\xi}+\frac{1}{2})\partial_x\phi^j(\xi)\mathrm{d}\xi \\ &\quad - \exp(\mathcal{I}m_1\omega)\int_{\hat{\xi}}^{\frac{1}{2}}\phi^l(\xi-\hat{\xi}-\frac{1}{2})\partial_x\phi^j(\xi)\mathrm{d}\xi. \end{aligned} \tag{C.12}$$

According to (C.5), there exists $\boldsymbol{S}=\sum_{\alpha=1}^{N_v}\boldsymbol{B}_\alpha$ and $\boldsymbol{B}_\alpha(\omega,\frac{\Delta t}{\varepsilon h};w_\alpha,v_\alpha)$ $(1\le\alpha\le N_v)$, such that

$$b_{I_i}(\langle vS_v^n[g_h^n]\rangle,\phi_i^j)=\exp(\mathcal{I}\kappa x_i)\sum_{\alpha=1}^{N_v}\sum_{l=0}^{q-1}B_{j,l,\alpha}(\omega,\frac{\Delta t}{\varepsilon h};w_\alpha,v_\alpha)\widehat{g}_l^n. \tag{C.13}$$

Similarly, there exists $\boldsymbol{C}_\alpha(\omega,\frac{\Delta t}{\varepsilon h};v_\alpha)\in\mathbb{R}^{q\times q}$, such that

$$a_{I_i}(f_h^n(\cdot,v),\phi_i^j)=\exp(\mathcal{I}\kappa x_i)\sum_{l=0}^{k-1}C_{j,l,\alpha}(\omega,\frac{\Delta t}{\varepsilon h};v_\alpha)\widehat{f}_l^n. \tag{C.14}$$

Now, we can write the SL1-LDGq method as (4.3) with $\boldsymbol{A}^{1,q}=(\boldsymbol{A}_L^{1,q})^{-1}\boldsymbol{A}_R^{1,q}$, where

$$\boldsymbol{A}_L^{1,q}=\begin{pmatrix} \boldsymbol{I}-c_2\boldsymbol{L}\boldsymbol{D} & 0 & 0 & 0\\ -c_4\boldsymbol{I} & \boldsymbol{I} & 0 & 0\\ -c_4\boldsymbol{I} & 0 & \boldsymbol{I} & 0\\ 0 & -\frac{1}{2}\boldsymbol{I} & -\frac{1}{2}\boldsymbol{I} & \boldsymbol{I}\end{pmatrix},\quad \boldsymbol{A}_R^{1,q}=\begin{pmatrix} 0 & c_1\boldsymbol{B}_1 & c_1\boldsymbol{B}_2 & -c_1\boldsymbol{S}\\ 0 & c_3\boldsymbol{C}_1 & 0 & 0\\ 0 & 0 & c_3\boldsymbol{C}_2 & 0\\ 0 & 0 & 0 & 0\end{pmatrix}. \tag{C.15}$$

$\boldsymbol{I}$ is the identity matrix and

$$\begin{aligned} c_1&=\frac{\Delta t}{\varepsilon h}\exp\left(-\frac{\Delta t}{\varepsilon^2}\right)=\frac{\Delta t}{\varepsilon h}\exp\left(-\frac{\Delta t/(\varepsilon h)}{\varepsilon/h}\right),\\ c_2&=\frac{\Delta t}{h^2}\left(1-\exp\left(-\frac{\Delta t}{\varepsilon^2}\right)\right)=\frac{\Delta t}{\varepsilon h}\left(1-\exp\left(-\frac{\Delta t/(\varepsilon h)}{\varepsilon/h}\right)\right),\\ c_3&=\frac{\varepsilon^2}{\varepsilon^2+\Delta t}=\frac{\varepsilon/h}{\varepsilon/h+\Delta t/(\varepsilon h)},\\ c_4&=\frac{\Delta t}{\varepsilon^2+\Delta t}=\frac{\Delta t/(\varepsilon h)}{\varepsilon/h+\Delta t/(\varepsilon h)}. \end{aligned} \tag{C.16}$$

This implies that $\boldsymbol{A}^{1,q}$ depends only on $\frac{\varepsilon}{h}$ and $\frac{\Delta t}{\varepsilon h}$. For the SL2-LDG$q$ method (3.33), we can carry out a similar analysis as above. We can obtain $\boldsymbol{A}^{2,q}=(\boldsymbol{A}_L^{2,q})^{-1}\boldsymbol{A}_R^{2,q}$, where

$$\begin{aligned} \boldsymbol{A}_L^{2,q}&=\begin{pmatrix} 3\boldsymbol{I}-2c_2\boldsymbol{L}\boldsymbol{D} & 0 & 0 & 0 & 0\\ -c_6\boldsymbol{I} & \boldsymbol{I} & 0 & 0 & 0\\ -c_6\boldsymbol{I} & 0 & \boldsymbol{I} & 0 & 0\\ 0 & -\frac{1}{2}\boldsymbol{I} & -\frac{1}{2}\boldsymbol{I} & \boldsymbol{I} & 0\\ 0 & 0 & 0 & 0 & \boldsymbol{I}\end{pmatrix},\\ \boldsymbol{A}_R^{2,q}&=\begin{pmatrix} 0 & 2c_1\boldsymbol{B}_1 & 2c_1\boldsymbol{B}_2 & 4\boldsymbol{I}-2c_1\boldsymbol{S} & -\boldsymbol{I}\\ 0 & (c_5-c_6)\boldsymbol{C}_1 & 0 & c_6\boldsymbol{C}_1 & 0\\ 0 & 0 & (c_5-c_6)\boldsymbol{C}_2 & c_6\boldsymbol{C}_2 & 0\\ 0 & 0 & 0 & 0 & 0\\ 0 & 0 & 0 & \boldsymbol{I} & 0\end{pmatrix},\\ c_5&=\frac{2\varepsilon^2}{2\varepsilon^2+\Delta t}=\frac{2\varepsilon/h}{2\varepsilon/h+\Delta t/(\varepsilon h)},\\ c_6&=\frac{\Delta t}{2\varepsilon^2+\Delta t}=\frac{\Delta t/(\varepsilon h)}{2\varepsilon/h+\Delta t/(\varepsilon h)}. \quad \square \end{aligned} \tag{C.17}$$

References

[1] S. Chandrasekhar, Radiative Transfer, Dover Publications, 1960.
[2] M. Modest, Radiative Heat Transfer, Academic Press, 2013.
[3] E.W. Larsen, J.E. Morel, W.F. Miller Jr, Asymptotic solutions of numerical transport problems in optically thick, diffusive regimes, J. Comput. Phys. 69 (2) (1987) 283–324.
[4] R.B. Pember, Numerical methods for hyperbolic conservation laws with stiff relaxation I. Spurious solutions, SIAM J. Appl. Math. 53 (5) (1993) 1293–1330.
[5] G. Naldi, L. Pareschi, Numerical schemes for kinetic equations in diffusive regimes, Appl. Math. Lett. 11 (2) (1998) 29–35.
[6] S. Jin, L. Pareschi, G. Toscani, Diffusive relaxation schemes for multiscale discrete-velocity kinetic equations, SIAM J. Numer. Anal. 35 (6) (1998) 2405–2439.
[7] S. Jin, Asymptotic preserving (AP) schemes for multiscale kinetic and hyperbolic equations: a review, in: Lecture Notes for Summer School on Methods and Models of Kinetic Theory (M&MKT), Porto Ercole (Grosseto, Italy), 2010, pp. 177–216.
[8] S. Jin, Asymptotic-preserving schemes for multiscale physical problems, Acta Numer. 31 (2022) 415–489.
[9] S. Jin, L. Pareschi, G. Toscani, Uniformly accurate diffusive relaxation schemes for multiscale transport equations, SIAM J. Numer. Anal. 38 (3) (2000) 913–936.
[10] S. Boscarino, L. Pareschi, G. Russo, Implicit-Explicit Runge–Kutta schemes for hyperbolic systems and kinetic equations in the diffusion limit, SIAM J. Sci. Comput. 35 (1) (2013) A22–A51.
[11] F. Filbet, S. Jin, A class of asymptotic-preserving schemes for kinetic equations and related problems with stiff sources, J. Comput. Phys. 229 (20) (2010) 7625–7648.
[12] M. Lemou, L. Mieussens, A new asymptotic preserving scheme based on micro-macro formulation for linear kinetic equations in the diffusion limit, SIAM J. Sci. Comput. 31 (1) (2008) 334–368.
[13] J. Jang, F. Li, J.-M. Qiu, T. Xiong, High order asymptotic preserving DG-IMEX schemes for discrete-velocity kinetic equations in a diffusive scaling, J. Comput. Phys. 281 (2015) 199–224.
[14] G. Dimarco, L. Pareschi, Exponential Runge-Kutta methods for stiff kinetic equations, SIAM J. Numer. Anal. 49 (5) (2011) 2057–2077.
[15] L. Mieussens, On the asymptotic preserving property of the unified gas kinetic scheme for the diffusion limit of linear kinetic models, J. Comput. Phys. 253 (2013) 138–156.
[16] W. Sun, S. Jiang, K. Xu, An asymptotic preserving unified gas kinetic scheme for gray radiative transfer equations, J. Comput. Phys. 285 (2015) 265–279.
[17] S. Jin, Runge-Kutta methods for hyperbolic conservation laws with stiff relaxation terms, J. Comput. Phys. 122 (1) (1995) 51–67.
[18] R.E. Caflisch, S. Jin, G. Russo, Uniformly accurate schemes for hyperbolic systems with relaxation, SIAM J. Numer. Anal. 34 (1) (1997) 246–281.
[19] A. Klar, An asymptotic-induced scheme for nonstationary transport equations in the diffusive limit, SIAM J. Numer. Anal. 35 (3) (1998) 1073–1094.
[20] A. Klar, A. Unterreiter, Uniform stability of a finite difference scheme for transport equations in diffusive regimes, SIAM J. Numer. Anal. 40 (3) (2002) 891–913.
[21] J.-G. Liu, L. Mieussens, Analysis of an asymptotic preserving scheme for linear kinetic equations in the diffusion limit, SIAM J. Numer. Anal. 48 (4) (2010) 1474–1491.

[22] J. Jang, F. Li, J.-M. Qiu, T. Xiong, Analysis of asymptotic preserving DG-IMEX schemes for linear kinetic transport equations in a diffusive scaling, SIAM J. Numer. Anal. 52 (4) (2014) 2048–2072.
[23] Z. Peng, Y. Cheng, J.-M. Qiu, F. Li, Stability-enhanced AP IMEX-LDG schemes for linear kinetic transport equations under a diffusive scaling, J. Comput. Phys. 415 (2020) 109485.
[24] T. Xiong, W. Sun, Y. Shi, P. Song, High order asymptotic preserving discontinuous Galerkin methods for gray radiative transfer equations, J. Comput. Phys. 463 (2022) 111308.
[25] A. Crestetto, N. Crouseilles, G. Dimarco, M. Lemou, Asymptotically complexity diminishing schemes (ACDS) for kinetic equations in the diffusive scaling, J. Comput. Phys. 394 (2019) 243–262.
[26] Z. Peng, F. Li, Asymptotic preserving IMEX-DG-S schemes for linear kinetic transport equations based on Schur complement, SIAM J. Sci. Comput. 43 (2) (2021) A1194–A1220.
[27] G. Zhang, H. Zhu, T. Xiong, Asymptotic preserving and uniformly unconditionally stable finite difference schemes for kinetic transport equations, SIAM J. Sci. Comput. 45 (5) (2023) B697–B730.
[28] K.D. Lathrop, Ray effects in discrete ordinates equations, Nucl. Sci. Eng. 32 (1968) 357–369.
[29] Y. Azmy, E. Sartori, Nuclear Computational Science-A Century in Review, Springer, 2010.
[30] Y. Shi, P. Song, T. Xiong, An efficient asymptotic preserving Monte Carlo method for radiative transfer equations, J. Comput. Phys. 493 (2023) 112483.
[31] W.H. Reed, T.R. Hill, Triangular mesh methods for the neutron transport equation, Tech. Rep., Los Alamos Scientific Lab., N. Mex. (USA), 1973.
[32] B. Cockburn, G.E. Karniadakis, C.-W. Shu, The Development of Discontinuous Galerkin Methods, Springer, 2000.
[33] C.-W. Shu, Discontinuous Galerkin methods: general approach and stability, Numer. Solut. Partial Differ. Equ. 201 (2009) 149–201.
[34] C.-W. Shu, Discontinuous Galerkin methods for time-dependent convection dominated problems: basics, recent developments and comparison with other methods, in: G.R. Barrenechea, F. Brezzi, A. Cangiani, E.H. Georgoulis (Eds.), Building Bridges: Connections and Challenges in Modern Approaches to Numerical Partial Differential Equations, in: Lecture Notes in Computational Science and Engineering, Springer International Publishing, 2016, pp. 371–399.
[35] P. Castillo, B. Cockburn, D. Schötzau, C. Schwab, Optimal a priori error estimates for the hp-version of the local discontinuous Galerkin method for convection–diffusion problems, Math. Comput. 71 (238) (2002) 455–478.
[36] J.-F. Remacle, J.E. Flaherty, M.S. Shephard, An adaptive discontinuous Galerkin technique with an orthogonal basis applied to compressible flow problems, SIAM Rev. 45 (1) (2003) 53–72.
[37] R. Biswas, K.D. Devine, J.E. Flaherty, Parallel, adaptive finite element methods for conservation laws, Appl. Numer. Math. 14 (1–3) (1994) 255–283.
[38] A. Cangiani, E.H. Georgoulis, P. Houston, hp-Version discontinuous Galerkin methods on polygonal and polyhedral meshes, Math. Models Methods Appl. Sci. 24 (10) (2014) 2009–2041.
[39] G. Russo, F. Filbet, Semi-Lagrangian schemes applied to moving boundary problems for the BGK model of rarefied gas dynamics, Kinet. Relat. Models 2 (1) (2009) 231–250.
[40] G. Russo, P. Santagati, S.-B. Yun, Convergence of a semi-Lagrangian scheme for the BGK model of the Boltzmann equation, SIAM J. Numer. Anal. 50 (3) (2012) 1111–1135.
[41] X. Cai, W. Guo, J.-M. Qiu, A high order conservative semi-Lagrangian discontinuous Galerkin method for two-dimensional transport simulations, J. Sci. Comput. 73 (2) (2017) 514–542.
[42] X. Cai, W. Guo, J.-M. Qiu, Comparison of semi-Lagrangian discontinuous Galerkin schemes for linear and nonlinear transport simulations, Commun. Appl. Math. Comput. (2020) 1–31.
[43] J. Lu, Y. Liu, C.-W. Shu, An oscillation-free discontinuous Galerkin method for scalar hyperbolic conservation laws, SIAM J. Numer. Anal. 59 (3) (2021) 1299–1324.
[44] Y. Liu, J. Lu, C.-W. Shu, An essentially oscillation-free discontinuous Galerkin method for hyperbolic systems, SIAM J. Sci. Comput. 44 (1) (2022) A230–A259.
[45] Z. Peng, Y. Cheng, J.-M. Qiu, F. Li, Stability-enhanced AP IMEX1-LDG method: energy-based stability and rigorous AP property, SIAM J. Numer. Anal. 59 (2) (2021) 925–954.
[46] R.K. Osborn, S. Yip, The Foundations of Neutron Transport Theory, Oct. 1963, http://deepblue.lib.umich.edu/handle/2027.42/93612.
[47] L. Ryzhik, G. Papanicolaou, J.B. Keller, Transport equations for elastic and other waves in random media, Wave Motion 24 (4) (1996) 327–370.
[48] W. Guo, R.D. Nair, J.-M. Qiu, A conservative semi-Lagrangian discontinuous Galerkin scheme on the cubed sphere, Mon. Weather Rev. 142 (1) (2014) 457–475.
[49] G.C. Pomraning, The Equations of Radiation Hydrodynamics, International Series of Monographs in Natural Philosophy, Pergamon Press, Oxford, 1973.
[50] V.I. Lebedev, Quadratures on a sphere, USSR Comput. Math. Math. Phys. 16 (2) (1976) 10–24.
[51] L. Einkemmer, J. Hu, Y. Wang, An asymptotic-preserving dynamical low-rank method for the multi-scale multi-dimensional linear transport equation, J. Comput. Phys. 439 (2021) 110353.
[52] B. Seibold, M. Frank, StaRMAP—a second order staggered grid method for spherical harmonics moment equations of radiative transfer, ACM Trans. Math. Softw. 41 (1) (2014) 1–28.
[53] R.G. McClarren, C.D. Hauck, Robust and accurate filtered spherical harmonics expansions for radiative transfer, J. Comput. Phys. 229 (16) (2010) 5597–5614.
[54] D. Radice, E. Abdikamalov, L. Rezzolla, C.D. Ott, A new spherical harmonics scheme for multi-dimensional radiation transport I. Static matter configurations, J. Comput. Phys. 242 (2013) 648–669.
[55] C.K. Garrett, C.D. Hauck, A comparison of moment closures for linear kinetic transport equations: the line source benchmark, Transp. Theory Stat. Phys. 42 (6–7) (2013) 203–235.
[56] M.P. Laiu, M. Frank, C.D. Hauck, A positive asymptotic-preserving scheme for linear kinetic transport equations, SIAM J. Sci. Comput. 41 (3) (2019) A1500–A1526.
[57] B.D. Ganapol, R.S. Baker, J.A. Dahl, R.E. Alcouffe, Homogeneous infinite media time-dependent analytical benchmarks, Los Alamos National Laboratory, 2001.
[58] W. Bennett, R.G. McClarren, Benchmarks for infinite medium, time dependent transport problems with isotropic scattering, J. Comput. Theor. Transp. 51 (4) (2022) 205–221.
[59] Benjamin Seibold, Martin Frank, Rujeko Chinomona, STARMAP, https://github.com/starmap-project/starmap, 2022.
[60] S. Ristov, M. Gusev, Superlinear speedup for matrix multiplication, in: Proceedings of the ITI 2012 34th International Conference on Information Technology Interfaces, IEEE, 2012, pp. 499–504.
[61] B. Yan, R.A. Regueiro, Superlinear speedup phenomenon in parallel 3D discrete element method (DEM) simulations of complex-shaped particles, Parallel Comput. 75 (2018) 61–87.